Three-Dimensional PET Emission Scan Registration and Transmission Scan Synthesis

Chung-Lin Huang,* *Member, IEEE*, Wen-Tsang Chang, Liang-Chih Wu, and Jiunn-Kuen Wang

***Abstract*— The duration of a positron emission tomography (PET) imaging scan can be reduced if the transmission scan of one patient which is used for emission correction can be synthesized by using the reference transmission scan of another patient. In this paper, we propose a new intersubjects PET emission scan registration method and PET transmission synthesis method by using the boundary information of the body or brain scan of the PET emission scans. The PET emission scans have poor image quality and different intensity statistics so that we preprocess the emission scans to have similar histogram and then apply the point distribution model (PDM) [15] to extract the contours of the emission scan. The extracted boundary contour of every slice is used to reconstruct the three-dimensional (3-D) surface of the reference set and the target set. Our registration is 3-D surface-based which uses the normal flow method [17] to find the correspondence vector field between two 3-D reconstructed surfaces. Since it is difficult to analyze internal organ using the PET emission scan imaging without correction, we assume that the deformation of internal organ is homogeneous. With the corresponding vector field between the two emission scans and the transmission scan of the reference set, we can synthesize the transmission scan of the target set.**

I. Introduction

POSITRON emission tomography (PET) is a nuclear medical imaging technique capable of providing quantitative functional information in intact human objects. PET often requires anatomic reference information (i.e., transmission scan obtained on the same object) to perform accurate attenuation correction of fluoro-deoxy-glucose (FDG) emission scan images. Therefore, during cardiac FDG PET imaging, the patient needs to be remain stationary on the scanning table for the transmission scan, the FDG injection, the 30–40 min wait, and finally the emission scan. The PET imaging system requires that the misalignment between the emission scan and the transmission scan be negligible. Therefore, the patient has to lie on the scan table without moving for over an hour. Patient discomfort can be reduced if the transmission scan session is replaceable. However, it is not acceptable to use the reference transmission scan to correct the target emission scan directly, because they not only have spatial displacement but also differ in the body shape.

Therefore, if we can find a synthesized target transmission scan for the target emission scan correction session, then the target transmission scan session is not required. By using the emission scan alignment from two different subjects, we may synthesize the target transmission scan using the reference transmission scan. Here we assume that the misalignment between the transmission scan and the emission scan imaging of the designated subject is adjustable. McCord *et al*. [7] have studied the effect of misalignment between PET emission and transmission scans. They studied the translation misalignment (left shift or right shift) of the PET scans of the same subject. In this paper, however, we develop a system to align two precorrected PET emission scans (without attenuation correction) from two different subjects and then to synthesize the target transmission scan using the reference transmission scan. Since it is difficult to analyze internal organ using the precorrected PET emission scan, we assume that the deformation of internal organ is homogeneous.

Image registration methods can be classified from different points of views: intrasubject with the same image modality, intrasubject with multimodality and intersubject with multimodality. In the intrasubject registration with the same modality, the subject can be viewed as a rigid body, and the main purpose of these methods is to find changes in the patient's condition. Herbin *et al*. [1] propose a six-parameter two-dimensional (2-D) registration model consisting of a bidirectional translation, a rotation, a magnification, and a line transformation of the pixels in one image to match the pixels in the other image. Barber [2] proposes a registration of two images of the same organ taken from different radionuclide tracers to compare the regional uptake of the two tracers. He uses a coordinate transfer function (CTF) that maps the pixels in one image to those in the second image. Wood *et al*. [3] propose a registration method for three-dimensional (3-D) alignment which calculates the ratio of two images from voxel-to-voxel and then moves the image relative to one another to minimize the variation of this ratio across voxels iteratively. Bacharach *et al*. [4] describe a registration method for aligning the PET transmission scans of the same patient acquired at different time intervals, and using correlation coefficient between the stacks of slices to find the optimum alignment. Thevenaz *et al*. [5] propose a multiscale registration method. It uses a spline processing, based on a coarse-to-fine pyramid strategy, and performs minimization of the mean square difference of intensities between a reference

Manuscript received August 2, 1996; revised March 4, 1997. This work was supported by the National Science Council, Taiwan, R.O.C. under Grant NSC 86-2745–E007–012. The Associate Editor responsible for coordinating the review of this paper and recommending its publication was C. J. Thompson. *Asterisk indicates corresponding author.*

*C.-L. Huang is with the Institute of Electrical Engineering, National Tsing-Hua University, Hsin-Chu, Taiwan, ROC (e-mail: clhuang@nthu.edu.tw)

W.-T. Chang is with the Institute of Electrical Engineering, National Tsing-Hua University, Hsin-Chu, Taiwan, ROC.

L.-C. Wu and J.-K. Wang are with the National PET/Cyclotron Center, Department of Nuclear Medicine, Taipei Veterans General Hospital, Taipei, Taiwan, ROC.

Publisher Item Identifier S 0278-0062(97)07783-5.

and a test data set according to a variation of the iterative Marquardt–Levenberg scheme.

The intrasubject registration with multimodality is more difficult. Different imaging modalities have different pixel sizes, fields of view, slice thickness, and different image characteristics. The main purpose of these methods is to integrate the information of different image modalities. Pelizzari *et al*. [6] propose a surface-matching technique (a hat-and-head method) to register CT and MRI brain image scans. The model taken from the scan covering a larger volume of the patient takes the role of "head." The "hat" model is represented as a set of independent points. Then they minimize a nonlinear function [24] (which is the mean distance between "hat" points and "head" surface) to find the geometrical transformation.

Different from the "head and hat" method, Evan *et al*. [8] develop an algorithm to find the optimal transform between two ensembles of equivalent points, using 3-D image/graphics analysis package. Equivalent points in two image volumes are identified, either manually or via an adjustable computerized volume of interest (VOI) atlas. The MRI data are then resampled along planes parallel the PET planes and the two volumes overlaid using opacity-weighted composition. Alpert *et al*. [9] propose a method to register two sets of image data by converting the whole brain volume which are translated and rotated with respect to one another. Their technique is based on the classical theory of rigid bodies, employing as its basis, the principal axes transformation. Recently, Van den Elsen *et al*. [10] apply the differential operators in scale space to CT and MR images to produce feature images depicting "ridgeness," which are used for registration. Their method is restricted to match the brain images from the same patient under rigid transformation.

Intersubject registration with multimodality combines the tomographic images of different patients. Thurfjell *et al*. [11] use the computerized brain atlas to aid the interpolation of functional images by introducing anatomical information to serve as a tool in the merging of data from different imaging modalities and to facilitate the comparisons of data from different individuals by allowing the anatomical standardization of individual data. Lin [12] uses an elastic image-matching technique to the automatic registration process based on the assumption that the topological configuration of the brain is invariant among normal subjects while the shapes of individual brain structure differ. Davatzikos *et al*. [13] propose a two-stage nonlinear registration algorithm: 1) use an active contour algorithm to establish a length-preserving, one-to-one mapping between the cortical and the ventricular boundaries of two to-be-registered images, 2) generate 2-D transformation based on an elastic body deformation. Eberl *et al*. [14] propose an automatic interstudy image registration method for PET and single photon emission computed tomography (SPECT). Their technique iteratively reslice a misalignment data set until the sum of the absolute difference from the reference set is minimized.

The above studies have used brain images of different imaging modalities (CT, MRI, PET, etc.), but, here, we consider the PET images scanning between navel and midriff (each slice includes three parts: trunk in the middle, and two arms on left and right sides). It is more challenging than brain image slices. All PET studies were performed

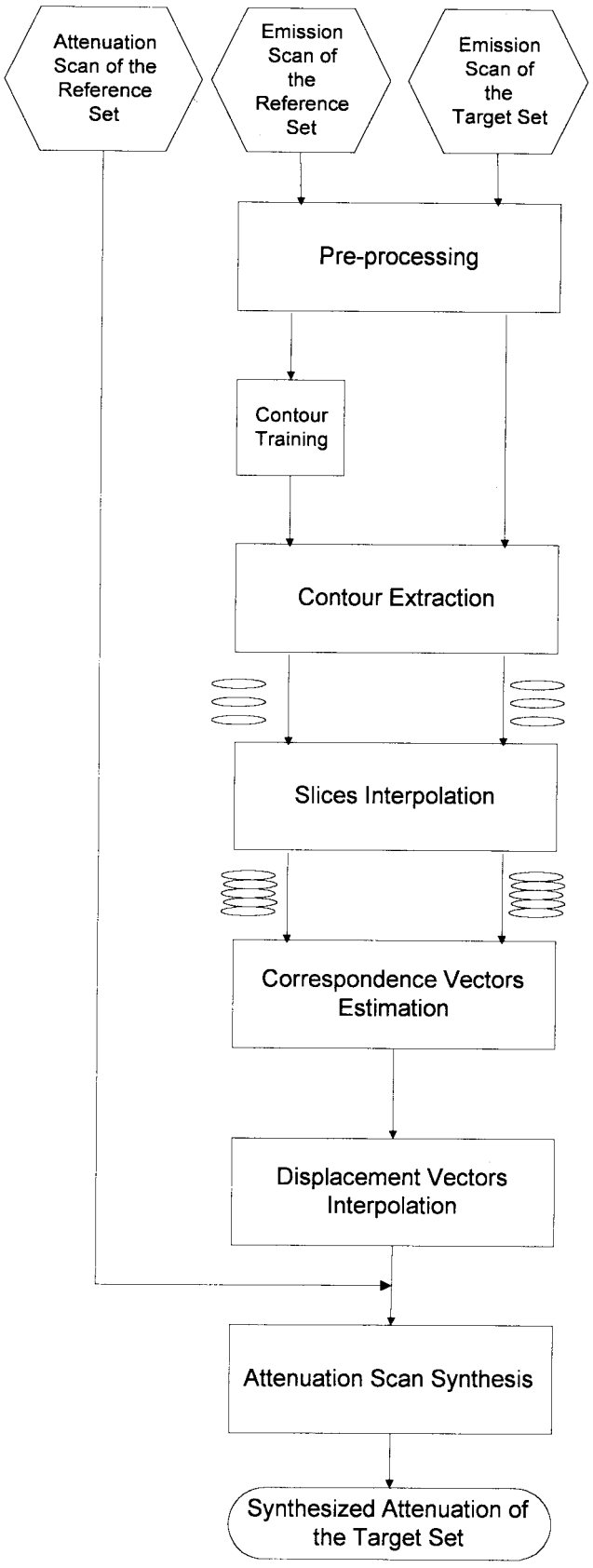

Fig. 1. The configuration of our system.

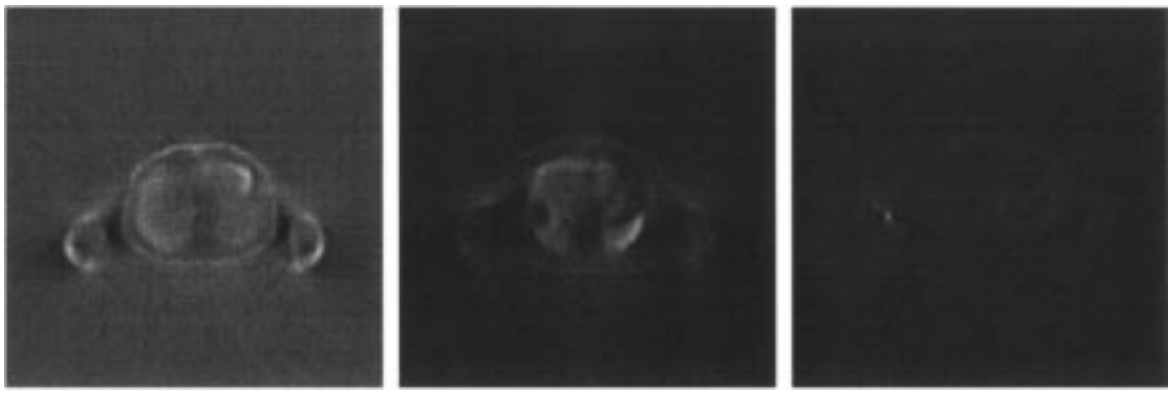

Fig. 2. Three examples of the original emission scan images.

on a GEMS-4096 15WB whole body tomography, a eight-ring system (made by Scanditronix, Uppsala, Sweden), which simultaneously acquires 15 slices with slice separation of 6.5 mm. Studies were constructed in a 128×128 matrix. The FDG-PET studies were collected for 20 min after a 50-min uptake period after injection of 10-mCi FDG. The data were reconstructed with a 4.2-mm Hanning filter (cutoff frequency 1.5 cycle/pixel and pixel size is 6 mm/pixel).

In this paper, given the reference set and target set of PET body scans (the former has both emission scan and transmission scan but the latter has emission scan only), we propose a new intersubject registration method to align the emission scan of the reference set and that of target set and then generate a set of correspondence vectors. We only select the similar FDG PET precorrected emission scan imaging for boundary registration because the emission scans themselves may be quite different, reflecting different conditions, (e.g., different drug, glucose loading, etc.). However, a similar FDG emission scan images may have quite different SNR and histogram. First, we need to preprocess the images to have similar histogram and SNR. Second, we use a point distribution model (PDM) [15], [16] to extract the boundary of the body cross section of the PET emission scan images. Third, we develop an interslice interpolation for 3-D surface reconstruction. Fourth, we apply the normal flow method [17] to find the correspondence between two sets of intersubject PET emission scan slices and generate a set of 3-D correspondence vectors. The registration method is fully 3-D with accurate intersubject alignment. Finally, by using the correspondence vectors and the transmission scan of the reference set, we can synthesize the transmission scan of the target set. The system flow diagram is illustrated in Fig. 1.

II. Boundary Extraction

Although similar FDG emission scan images from different patients are selected for registration in our system, the intensity characteristics of two sets of images from different patients are still quite different. Therefore, the boundary of the emission scan images are the only reliable information that we can apply for registration. Fig. 2 shows the original emission scan image. It is not easy even for our naked eyes to identify the trunk and two arms accurately. Here, we mention two image preprocessing algorithms: the histogram modification and the coarse segmentation which make the PET emission scan images have similar graylevel histograms and signal-to-noise ratio (SNR). Then, we apply the so-called PDM [15] to extract the boundary of the emission scan images.

A. Preprocessing

Because of the histogram difference of different precorrected PET emission scan images, the images blurs and low contrast, the contours of the PET images cannot be easily identified. We also find that the graylevel values of the pixels inside the body are a little higher than the graylevel values of the pixels outside the body. The purpose of preprocessing is to modify the histogram and then coarsely segment the images. Preprocessing is applied to the precorrected emission scans of both the reference set and the target set with the results shown in Figs. 3 and 4.

1) Histogram Modification: Histogram equalization [19] is an effective method to enhance the precorrected emission scan images, so that they will have similar histograms. The histogram equalization for discrete case is described as

$$s_k = T(r_k) = \sum_{j=0}^{k} \frac{n_j}{n} = \sum_{j=0}^{k} p_r(r_j) \tag{1}$$

where $0 \le r_k \le 1, k = 0, 1, \cdots, L-1, r_k$ is the original gray level, s_k is the transformed value, $p_r(r_j)$ is the probability density function, and L is the largest gray level (here, $L = 255$). The transformed value s_k is in the interval [0, 1], so, we use

$$g_k = 255 s_k \tag{2}$$

to rescale gray level g_k to the interval [0, 255].

2) Coarse Segmentation: After histogram equalization, most of the pixels of the enhanced image will have high illumination. The boundary of the body still cannot be easily identified from the enhanced image. By applying the multithresholdable image segmentation [23] which consists in looking for the bipoint corresponding to the normal of the most striking boundaries. We obtain the possible thresholds by taking the intervals defined by these bipoints. To obtain the best thresholds (t_1 and t_2), we look for separators which cut the intervals the best. In our experiment, we have determined

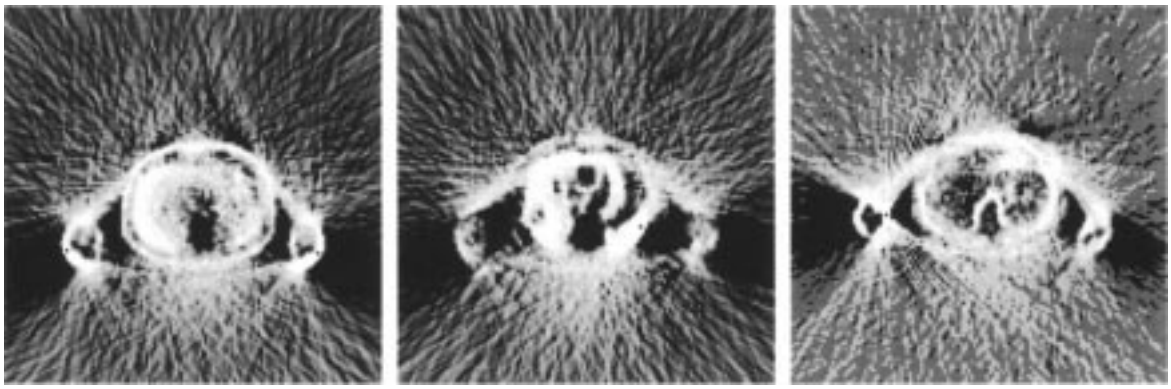

Fig. 3. The examples of the original images after histogram equalization.

Fig. 4. The segmentation results of the enhanced images.

the thresholds as $t_1 = 170$ and $t_2 = 215$ which are used for a coarse segmentation process to roughly segment the image based on the following pixel grouping:

$$\begin{aligned} &\text{if } g_k < 170, \qquad \text{then } g_k = 0 \\ &\text{else if } g_k < 215, \qquad \text{then } g_k = (2/3)g_k \\ &\text{else } g_k \text{ does not change.} \end{aligned} \tag{3}$$

The process are applicable for most PET emission scan images. Since most of the first group of pixels are either located outside the body or found outside the trunk, we may assign zero value for these pixels. For some pixels close to the body, we find their pixel values are between 170 and 215. The second group of pixels are located inside the trunk and close to the boundary so that they are applicable for the training process. We reduce the pixel intensity values of the second group of pixels so that they can be differentiated from the third group of pixels in the image. The third group of pixels in the image have graylevels larger than 215. Most of the third group of pixels are located on the boundary of the body.

B. PDM for Boundary Extraction

The PDM [15], [16] can be generated from a set of training examples, each represented by N variables. It requires a set of training images from which the average examples is calculated and the deviation of each example from the mean is established. A principal component analysis of the covariance matrix of deviations reveals the main mode of variation. Usually only a small number of model parameters is required to reconstruct the training examples. We may generate new examples of the shape, which will be similar to those in the training set, by varying the shape parameters within certain limits.

1) Training Set Processing: To extract the contour of the human body from the PET images, we need to establish a flexible model which can describe the typical shape and variability from the training sets. To achieve this, we will label some points at the boundary of the human body, then calculate the mean positions of these points and the parameters which may characterize the variations of these points.

a) Labeling the training set: The precorrected emission scan images are too blurred for human being to identify the boundary of the trunk. Here, we assume that the mismatch between the emission scan and the transmission scan of the reference set is negligible, so that we can use the transmission scan as an aid to manually label the points on the emission scan. There are eight points selected on the contour of each slice of the arm and 32 points selected on the boundary of each slice of the trunk as shown in Fig. 5. In the experiments, we have four reference sets and each set has 15 images, for a total of 60 images to be labeled as the training set.

b) Training shapes alignment: After labeling, the labeled points from different shapes must be aligned with respect to a set of axes. They are aligned by scaling, rotation, and translation so that they correspond as closely as possible. This alignment method is a modification of the Procrustes method

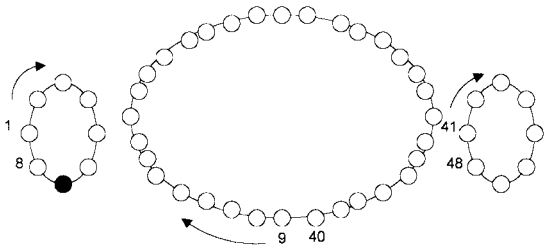

Fig. 5. The model of the boundary of a human body with 48 points.

[20]. Let $\boldsymbol{x}_i$ be a vector describing the n points of the ith shape in the training set as

$$\boldsymbol{x}_i = (x_{i0}, y_{i0}, x_{i1}, y_{i1}, \cdots, x_{ik}, y_{ik}, \cdots, x_{in-1}, y_{in-1})^T \quad (4)$$

Assume that we have two similar shapes, $\boldsymbol{x}_i$ and $\boldsymbol{x}_j$, and we are going to determine a rotation, θ, a scale, s, and two translation, t_x and t_y, mapping $\boldsymbol{x}_i$ onto $M(\boldsymbol{x}_j) + \boldsymbol{t}_j$. To minimize the weighted sum

$$E = (\boldsymbol{x}_i - \boldsymbol{M}(s,\theta)[\boldsymbol{x}_j] - \boldsymbol{t})^T \boldsymbol{W} (\boldsymbol{x}_i - \boldsymbol{M}(s,\theta)[\boldsymbol{x}_j] - \boldsymbol{t}) \quad (5)$$

where

$$\boldsymbol{M}(s,\theta)\begin{bmatrix} x_{jk} \\ y_{jk} \end{bmatrix} = \begin{pmatrix} (s\cos\theta)x_{jk} - (s\sin\theta)y_{jk} \\ (s\sin\theta)x_{jk} + (s\cos\theta)y_{jk} \end{pmatrix},$$
$$\boldsymbol{t} = (t, t_y, \cdots, t_x, t_y)^T$$

and $\boldsymbol{W}$ is a diagonal matrix of weights for each points. The replacement $a_x = s\cos\theta, a_y = s\sin\theta$ and a least-squares approach (differential respect to variables: a_x, a_y, t_x, t_y) lead to a set of four linear equations, which can be used to solve a_x, a_y, t_x, and t_y.

c) Capturing the statistics of aligned shapes: The equivalent points of the aligned shapes are scattered in the distribution regions of the so-called *allowable shape domain*. We use the PDM to model the variation of the distribution region. Given a set of N aligned shapes, the mean shape, $\overline{\boldsymbol{x}}$, is calculated from

$$\overline{\boldsymbol{x}} = \frac{1}{N}\sum_{i=1}^{N} \boldsymbol{x}_i \quad (6)$$

and the deviation from the mean $d\boldsymbol{x}_i = \boldsymbol{x}_i - \overline{\boldsymbol{x}}$. Then, we calculate the $2n \times 2n$ covariance matrix, $\boldsymbol{S}$, as

$$\boldsymbol{S} = \frac{1}{N}\sum_{i=1}^{N} d\boldsymbol{x}_i \, d\boldsymbol{x}_i^T. \quad (7)$$

The *allowable shape domain* can be viewed as an ellipsoid. The principal axes of the ellipsoid of the *allowable shape domain*, giving the modes of variation of the points of the shape, are described by $\boldsymbol{p}_k$ $(k = 1, \cdots 2n)$, the eigenvectors of $\boldsymbol{S}$

$$\boldsymbol{S}\boldsymbol{p}_k = \lambda_k \boldsymbol{p}_k \quad \text{with} \quad \boldsymbol{p}_k^T \boldsymbol{p}_k = 1 \quad (8)$$

where λ_k is the kth eigenvalue of $\boldsymbol{S}$ and $\lambda_k > \lambda_{k+1}$. The eigenvectors of the covariance matrix corresponding to the largest eigenvalue describes the longest axes of the ellipsoid, and the most significant modes of variation in the variables used to derive the covariance matrix.

Any points in the *allowable shape domain* can be presented by taking the mean and adding a linear combination of the eigenvectors

$$\boldsymbol{x} = \overline{\boldsymbol{x}} + \boldsymbol{P}\boldsymbol{b} \quad (9)$$

$\boldsymbol{P} = (\boldsymbol{p}_1, \cdots \boldsymbol{p}_n)^T$ is the matrix of the eigenvectors and $\boldsymbol{b} = (b_1, \cdots b_n)^T$ is a vector of weights. The above equation allows us to generate new shapes by varying the parameters b_k within suitable limits, and these new shapes are similar to those in the training set. Usually, the suitable limits are

$$-3\sqrt{\lambda_k} \le b_k \le 3\sqrt{\lambda_k}. \quad (10)$$

Alternatively, one can choose sets of parameters $\{b_1, \cdots b_n\}$ such that the Mahalanobis distance D_m from the mean is less than the maximum value, $D_{\max}$ as

$$D_m^2 = \sum_{k=1}^{n} \left(\frac{b_k^2}{\lambda_k}\right) \le D_{\max}^2. \quad (11)$$

2) Modeling Graylevel Profile: Attempting to fit to an image object with our models, we need to find the adjustment which will move each point toward a better position. The graylevel patterns about the labeled model points of different images are often similar. Here, we analyze the statistics of the graylevel profiles normal to curves passing through the points. Although, in some cases, it is sufficient to assume that the points lie on the strong edges and it is easy to search them in the images. However, this is not always true for PET emission scan images. It is necessary to generate a more general model of the graylevel profile. We extract a profile g_i of length n_p pixels which are centered at the point on the shape boundary of each training image.

The profile is the sample of the derivative of the graylevels along it which is normalized. This profile is uniform scaling-invariant and unbiased to the graylevel constant. Therefore, the mean profile $\overline{\boldsymbol{g}}$ and the covariance matrix $\boldsymbol{S}_g$ can be calculated, and we will have the first and second order statistical description of the profiles at the point. The variation about the mean profile is described by $\boldsymbol{P}_g$, the eigenvectors of $\boldsymbol{S}_g$, corresponding to the n_g $(\le n_p)$ largest eigenvalues.

In a new example of image the profile of the points can be written as

$$\boldsymbol{g}_{\text{new}} = \overline{\boldsymbol{g}} + \boldsymbol{p}_{\boldsymbol{g}} \boldsymbol{b}_{g(\text{new})} \quad (12)$$

where $\boldsymbol{b}_{g(\text{new})}$ is a set of n_g parameters describing the profile model. The *profile model* is given by $\overline{\boldsymbol{g}}, \boldsymbol{P}_g$ and the n_g largest eigenvalue $\lambda_j, j = 1, \cdots n_g$. We fit the *profile model* to *image profile* $\boldsymbol{g}$ with the central point g_{ik} and along the normal direction of the ith shape model point as

$$\boldsymbol{b}_g = \boldsymbol{P}_{\boldsymbol{g}}^T (\boldsymbol{g} - \overline{\boldsymbol{g}}) \quad (13)$$

we will get a set of $\boldsymbol{b}_g$, and then calculate how well the *profile model* fits the *image profile* by using the Mahalanobis distance as

$$M = \sum_{j=1}^{n_p} \frac{b_{gj}^2}{\lambda_j} \quad (14)$$

where λ_j is the eigenvalue corresponding to the jth eigenvector and $\lambda_j > \lambda_{j+1}$. By moving to different profile central point g_{ik} and do the same model-profile fitting, we may find the best-matched profile $\boldsymbol{b}_g$ which corresponds to the minimum M.

3) Contour Extraction by Computing the Changes: To extract the contour of the cross section of the precorrected PET emission image, we assign an initial shape model which is arbitrarily located close to the real contour of the cross section. The initial position of the shape model is given by

$$\boldsymbol{X} = \boldsymbol{M}(s,\theta)[\boldsymbol{x}] + \boldsymbol{X}_c \tag{15}$$

where $\boldsymbol{X}_c = (X_c, Y_c, \cdots X_c, Y_c)^T$ and $M(s,\theta)[\cdot]$ is a rotation and a scaling operation, and (X_c, Y_c) is the position of the center of the model in the image.

After searching the best-matched profiles for all model points in a image of the target set, an adjustment vector $d\boldsymbol{X} = (dX_0, dY_0, \cdots, dX_{n-1}, dY_{n-1})^T$ will be generated. The adjustment vector cannot add on the initial model position $\boldsymbol{X}$ directly, because it does not satisfy the shape constraint of the model. Therefore, we will find the translation (dX_c, dY_c), the rotation $d\theta$, and a scaling factor $(1+ds)$ after best-match and map $\boldsymbol{X}$ onto $(\boldsymbol{X} + d\boldsymbol{X})$. Then, we calculate the residual adjustments $d\boldsymbol{x}$ which can be satisfied by deforming the shape of the model in the local coordinate frame as

$$\begin{aligned}\boldsymbol{M}(s(1+ds),(\theta+d\theta))[\boldsymbol{x}+d\boldsymbol{x}] + (\boldsymbol{X}_c + d\boldsymbol{X}_c) \\ = (\boldsymbol{X} + d\boldsymbol{X}).\end{aligned} \tag{16}$$

Substituting (15) to (16) we have

$$\begin{aligned}\boldsymbol{M}(s(1+ds),(\theta+d\theta))[\boldsymbol{x}+d\boldsymbol{x}] \\ = (\boldsymbol{M}(s,\theta)[\boldsymbol{x}] + d\boldsymbol{X}) - (\boldsymbol{X}_c + d\boldsymbol{X}_c)\end{aligned} \tag{17}$$

since $\boldsymbol{M}^{-1}(s,\theta)[\cdot] = \boldsymbol{M}(s^{-1}, -\theta)[\cdot]$ we can obtain

$$d\boldsymbol{x} = \boldsymbol{M}((s(1+ds))^{-1}, -(\theta+d\theta))[\boldsymbol{y}] - \boldsymbol{x} \tag{18}$$

where $\boldsymbol{y} = \boldsymbol{M}(s,\theta)[\boldsymbol{x}] + d\boldsymbol{X} - d\boldsymbol{X}_c$ and we need to use the shape constraint, so from (9), we can find $d\boldsymbol{b}$ such that

$$\boldsymbol{x} + d\boldsymbol{x} \approx \overline{\boldsymbol{x}} + \boldsymbol{P}(\boldsymbol{b} + d\boldsymbol{b}). \tag{19}$$

Subtracting (9) from (19), we have

$$d\boldsymbol{x} + \boldsymbol{P}(d\boldsymbol{b}) \quad \text{or} \quad d\boldsymbol{b} + \boldsymbol{P}^T d\boldsymbol{x} \tag{20}$$

since $\boldsymbol{P}^T = \boldsymbol{P}^{-1}$, as the columns of $\boldsymbol{P}$ are mutually orthogonal and are unitary vectors. The above equations allow us to calculate the changes of the position variables and adjustments, dX_c, dY_c, $d\theta$, and ds, to the shape parameters $d\boldsymbol{b}$ required to improve the match between an object model and image evidence. We can update the parameters iteratively by $X_c = X_c + dX_c, Y_c = Y_c + dY_c, \theta = \theta + d\theta, s = s(1+ds), \boldsymbol{b} = \boldsymbol{b} + d\boldsymbol{b}$.

The shape is acceptable if the Mahalanobis distance D_m is less than the maximum value, $D_{\max}$ (11). If the updating $\boldsymbol{b}$ leads to an implausible shape, i.e., $D_m > D_{\max}, \boldsymbol{b}$ can be rescaled to the proper position by using $b_k \rightarrow b_k(D_{\max}/D_m)$, where $k = 1, \cdots n$. The searching and updating procedure is repeated until no significant change results.

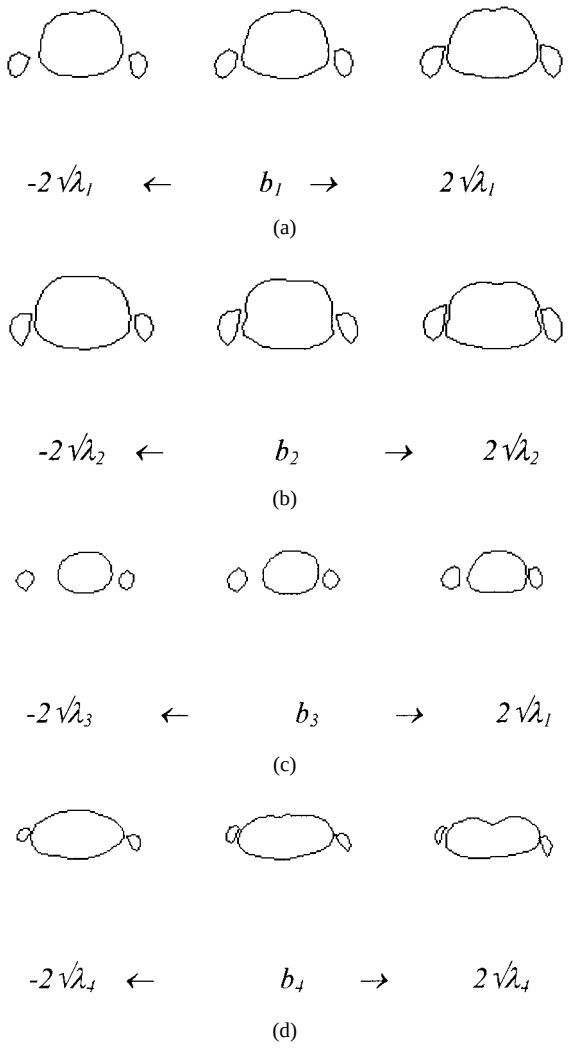

Fig. 6. Examples of body shapes in the training set, each containing 48 points.

C. The Experimental Results of Contour Extraction

The PET precorrected emission scan model was trained using a set of 60 examples of PET precorrected emission images taken from different subjects as the training set. Here, we only select the similar FDG PET emission scan imaging for boundary registration because the emission scans themselves may be quite different, reflecting different conditions (e.g., different drug, glucose loading, etc.), the training images would be adequately cover the range of morphology seen in FDG PET emission scans. When building shape models, it is important that the points are placed on the training images as accurately as possible, and the shapes are aligned similarly. Therefore, for each training emission scan example, we select 48 model points that are manually selected based on the corresponding transmission scan image of the same subject which has much higher contrast than the precorrected emission scan. In the experiments, we assume that the misalignment between the PET emission scan and the PET transmission scan of the same subject is negligible.

In Fig. 6, we illustrate the reconstructed cross-section contours by varying each of the first four model parameters, b_1, b_2,

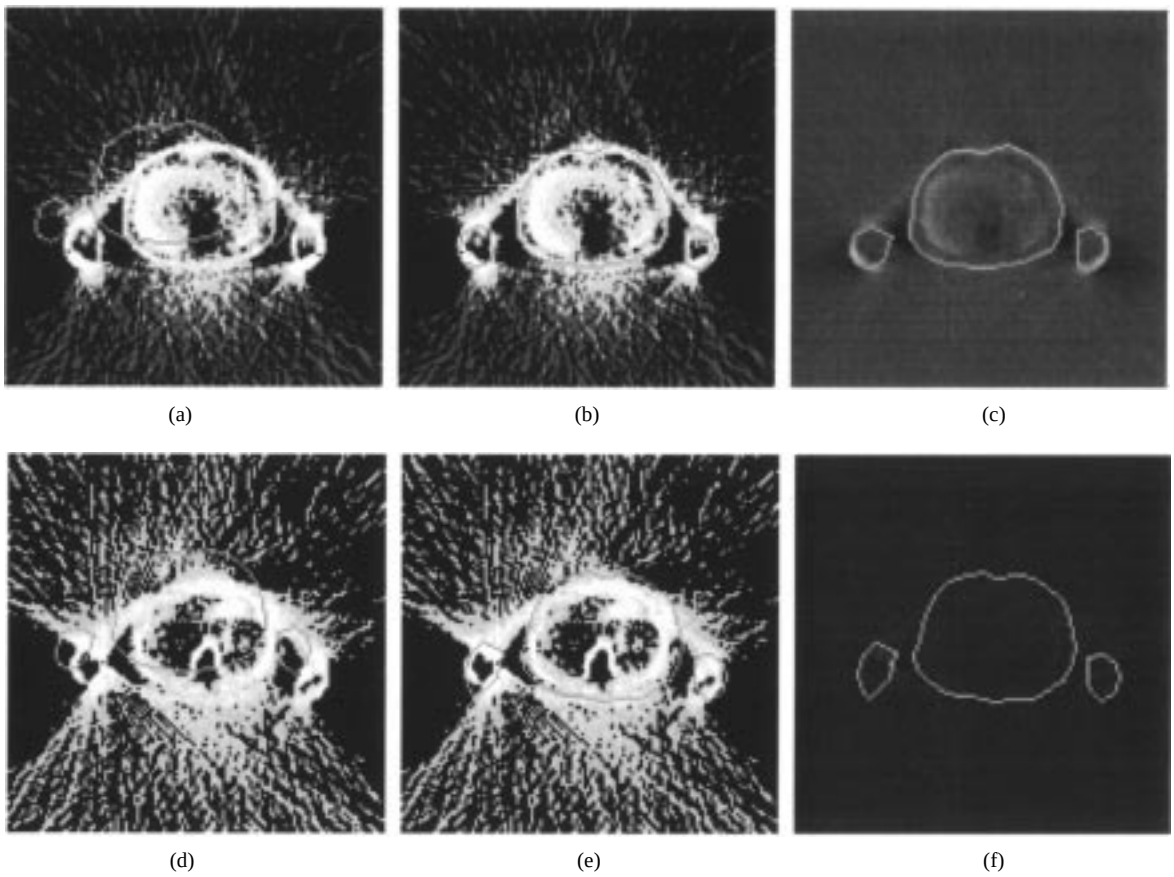

Fig. 7. The results of the boundary extraction in the reference sets and the target sets. (a) The initial position of the shape model in a preprocessed emission scan image of the reference set. (b) The extracted contour after 100 iterations. (c) The extracted contour in the original emission scan image. (d) The initial position in an preprocessed emission scan image of the target set. (e) The extracted contour after 100 iterations. (f) The extracted contour in the original emission scan image.

b_3, and b_4 in turn, and keeping the others zero. This method has been applied successfully on the extracted contours of the PET emission images (see Fig. 7). The placement of the initial contour was obtained by choosing a set of position parameters closing to the region of interest and setting all the shape parameters zero (mean shape). After 100 iterations, the model gives a good fit to the data. Each iteration takes about 0.1 s for a Pentium CPU. From Fig. 7(c) and (f), we find that the correct arm contours are identified for different subjects.

III. Slices Interpolation

For the intersubject PET precorrected emission scan registration, we need to consider the misalignment in the z-axis. Since the contours extracted from two contiguous slices do not change smoothly, to obtain a more precise z-direction registration, we need to apply the elastic interpolation method [18] to interpolate contours between two continuous slices.

A. Elastic Interpolation

The elastic interpolation is treated as a deformed process between two similar contours, i.e.

$$\boldsymbol{C1} = \{(x1_i, y1_i) | 1 \le i \le N\}$$

and

$$\boldsymbol{C2} = \{(x2_i, y2_i) | 1 \le i \le N\} \tag{21}$$

where $\boldsymbol{C1}$ can be viewed as the start contour which is going to be deformed to the end contour $\boldsymbol{C2}$. Let $(x1_i, y1_i)$ and $(x2_i, y2_i)$ be the coordinates of the points i corresponding to the start contour and the end contour, and N be the number of points of each contour ($N = 8$ for arms and $N = 32$ for trunk).

First, we will measure the similarity of every point in $\boldsymbol{C1}$ with the point in $\boldsymbol{C2}$ and find a corresponding point on some line segment of $\boldsymbol{C2}$. There are two measurements. The first measurement is the *position difference measurement* which is defined as

$$\rho(i,j) = \frac{|\boldsymbol{A} \times \boldsymbol{B}|}{|\boldsymbol{B}|} = |\boldsymbol{A}| \sin\theta \tag{22}$$

where (1) $\boldsymbol{A}$ and $\boldsymbol{B}$ are two vectors defined as $\boldsymbol{A} = \boldsymbol{P1}(i) - \boldsymbol{P2}(j)$ and $\boldsymbol{B} = \boldsymbol{P2}(j+1) - \boldsymbol{P2}(j)$, (2) $\boldsymbol{P1}(i)$ and $\boldsymbol{P2}(i)$ are the locations corresponding to the points on two curves, i.e., $\boldsymbol{C1}$ and $\boldsymbol{C2}$, (3) θ is the angle between $\boldsymbol{A}$ and $\boldsymbol{B}$. This equation measures the shortest distance from every point in $\boldsymbol{C1}$ to every line segment in $\boldsymbol{C2}$. By minimizing $\rho(i,j)$, we can find the corresponding line segment in $\boldsymbol{C2}$ for every point in $\boldsymbol{C1}$. If the position difference measurement cannot find an unique line segment for some points in $\boldsymbol{C1}$, then we will use the *directional incompatibility measurement* to choose one

$$\vartheta(i,j) = \frac{|\boldsymbol{E} \times \boldsymbol{B}|}{|\boldsymbol{E}||\boldsymbol{B}|} = \sin\alpha \tag{23}$$

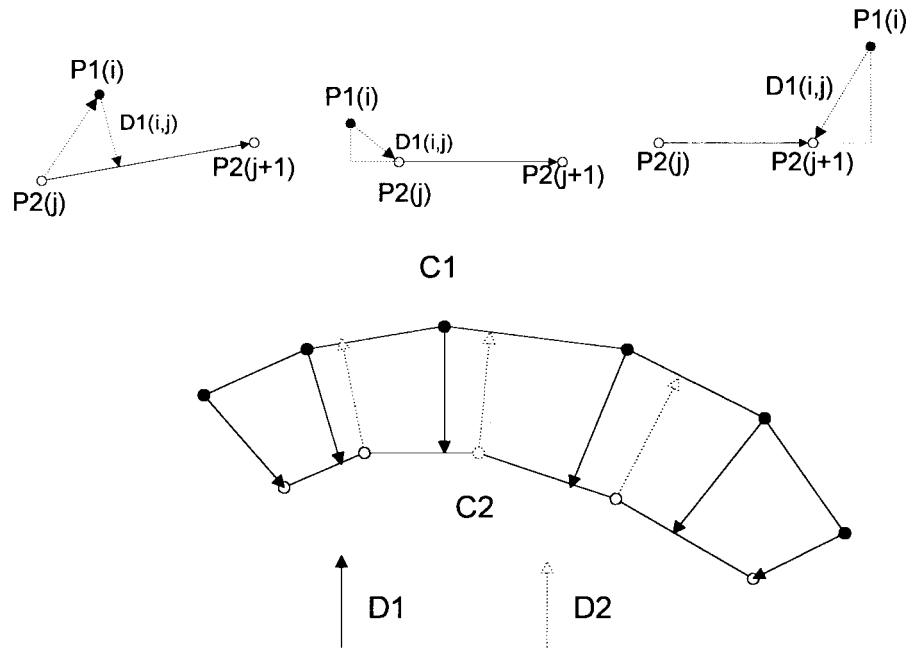

Fig. 8. Displacement vectors of two contours.

where α is the angle of the line segments $\boldsymbol{E}$ and $\boldsymbol{B}$ in $\boldsymbol{C1}$ and $\boldsymbol{C2}$, $\boldsymbol{E}$ is defined as $\boldsymbol{E} = \boldsymbol{P1}(i+1) - \boldsymbol{P1}(i)$ and $\boldsymbol{B}$ is defined in (22). If the two line segments are parallel, the directional incompatibility is zero. It is equal to one when they are orthogonal. Then, the displacement vectors can be determined by

$$\boldsymbol{D1}(i,j) = \begin{cases} |\boldsymbol{A}| \sin\theta * \boldsymbol{n12} \\ \quad \text{if } 0 \le |\boldsymbol{A}| \cos\theta \le |\boldsymbol{B}| \\ \boldsymbol{P2}'(j) - \boldsymbol{P1}(i) \\ \quad \text{if } |\boldsymbol{A}| \cos\theta \ge |\boldsymbol{B}| \text{ or } |\boldsymbol{A}| \cos\theta < 0 \end{cases} \tag{24}$$

$\boldsymbol{n12}$ is the unit vector parallel to the shortest distance point to line segment and $\boldsymbol{P2}'(j)$ may be the point $\boldsymbol{P2}(j)$ or $\boldsymbol{P2}(j+1)$ whichever is closer to $\boldsymbol{P1}(i)$. Reversing the roles of the start and end contours, the displacement vector $\boldsymbol{D2}(i,j)$ is defined at each point $\boldsymbol{P2}(i)$ in $\boldsymbol{C2}$. Fig. 8 shows the displacement vectors of both directions from $\boldsymbol{C1}$ and $\boldsymbol{C2}$.

The minimum displacement vectors $\boldsymbol{D1}(i, \boldsymbol{J}_i)$ can be viewed as the force pulling $\boldsymbol{C1}$ to $\boldsymbol{C2}$ and $\boldsymbol{D2}(j, \boldsymbol{I}_j)$ as the pushing force, they are defined as $\boldsymbol{D1}(i, \boldsymbol{J}_i) = \min_j \boldsymbol{D1}(i,j)$ and $\boldsymbol{D2}(j, \boldsymbol{I}_j) = \min_i \boldsymbol{D2}(j,i)$. The neighboring vectors must be taken into consideration. So, a Gaussian weight function is used to smooth the force field and the closer vectors will be given more weight as they have more impact on the pushing force. The smooth displacement field is defined as a function of $\boldsymbol{D1}$ and $\boldsymbol{D2}$

$$\boldsymbol{DS}(x,y) = \frac{\sum_{i=1}^{N} G1_i \boldsymbol{D1}(i, \boldsymbol{J}_i)}{\sum_{i=1}^{N} G1_i} - \frac{\sum_{j=1}^{N} G2_j (\boldsymbol{D2}(j, \boldsymbol{I}_j)}{\sum_{j=1}^{N} G2_j} \tag{25}$$

where $G1$ and $G2$ are Gaussian weights defined as

$$G1_i = \exp \frac{-(x - x1_i)^2 - (y - y1_i)^2}{\sigma_k^2} \quad \text{and}$$
$$G2_j = \exp \frac{-(x - x1_j - D2_x)^2 - (y - y1_j - D2_y)^2}{\sigma_\kappa^2} \tag{26}$$

$D2_x$ and $D2_y$ are the x and y components of $\boldsymbol{D2}$, and σ_k will gradually decrease after each iteration. The iterative formula of finding interpolation contours is

$$\boldsymbol{C}^k(i) = \boldsymbol{C}^{k-1}(i) + \boldsymbol{DS}^{k-1}(x_i^{k-1}, y_i^{k-1}) \tag{27}$$

where the initial contour $\boldsymbol{C}^0 = \boldsymbol{C1}$. After each iteration, an interpolated contour will be generated. The iteration stops if after the kth iteration the interpolated contour $\boldsymbol{C}^k(i)$ approaches the goal contour $\boldsymbol{C2}$. The difference between the $\boldsymbol{C}^k(i)$ and $\boldsymbol{C2}$ is less than certain threshold, i.e., $\boldsymbol{C2} = \boldsymbol{C}^k(i) + \boldsymbol{DS}^k(x_i, y_i)$ and $\Sigma_k |\boldsymbol{DS}^k(x_i, y_i)| < \varepsilon$.

B. The Interpolation Results

Here, we use a synthesized cylindrical vase to verify this interpolation method. There are 15 slices of the original contours, and each contour has 30 selected points. We interpolate one slice between two continuous slices by using the displacement field $\boldsymbol{DS}$ and then extrapolate one slice after the 15th slice of the original contours by using the displacement field $\boldsymbol{DS}$ between the interpolated slice $14\frac{1}{2}$ and the slice 15. So, there will be 30 slices after interpolation. Fig. 9 shows the original cylinder and the interpolation result. Next, three contours of PET image need to be interpolated separately. The original contours of 15 slices are also interpolated into 30 slices which are shown in Fig. 10. The reconstructed 3-D

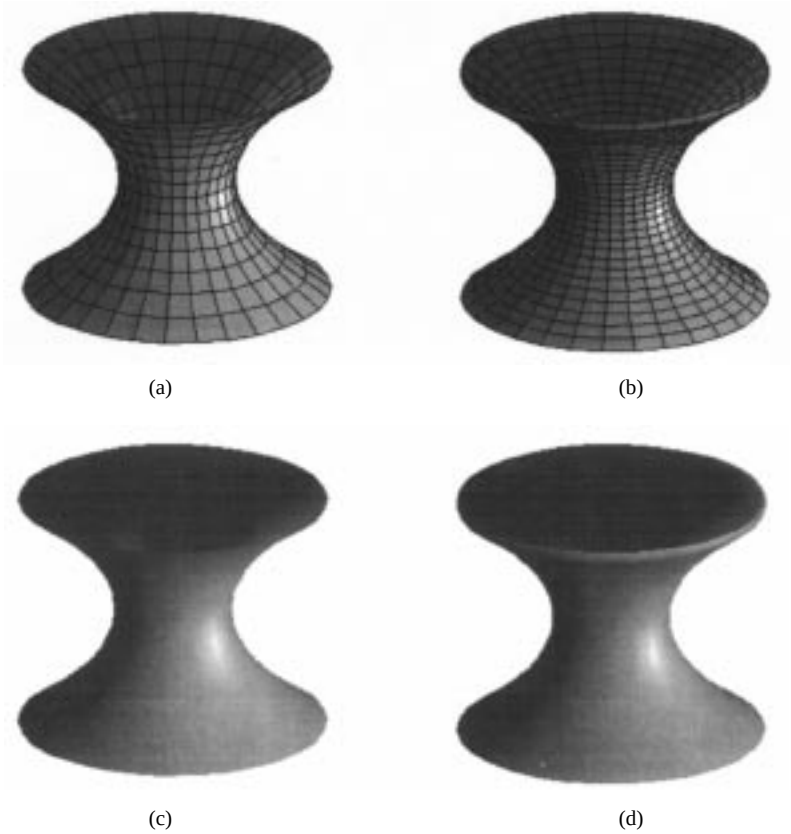

Fig. 9. (a) The original cylinder with grid. (b) The interpolated cylinder with grid. (c) The original cylinder after shading. (d) The interpolated cylinder after shading.

surfaces of the PET emission scans of the reference set and the target set are used in registration.

IV. Three-Dimensional Intersubject Registration

Here, we stack the 2-D contours of these slices and have two 3-D surfaces for reference set and target set. To solve the 3-D elastic boundary registration between the reference and the target PET emission scans, first, we calculate the normal vector of each surface patch on the boundary surface of PET emission scan. Second, we convert the 3-D normal vector field into 2-D vector frame which is treated as an 2-D image intensity frame. The variation of two sets of 3-D normal vector fields can be treated as two dynamic image frames of which the intensity of each pixel represents the normal of the corresponding surface voxel. Third, the registration between two sets of surface voxels can be solved by using normal flow method [17]. Fourth, the 2-D correspondence vectors are deprojected to 3-D correspondence vectors of each surface voxel. Finally, we can estimate the 3-D correspondence vector field which describes the registration of two objects.

A. Normal Vector Field

The normal direction on each surface patch with the center voxel located at (x_0, y_0, z_0) is calculated by using the neighboring surface voxels. A surface patch $S(x, y, z)$ can be described as the parametric representation $\boldsymbol{r}(u, v)$. Assume that the surface patch $S(x_0, y_0, z_0)$ is mapped to $\boldsymbol{r}(u_0, v_0)$. So, we can find two curves, $\boldsymbol{r}(u, v_0)$ and $\boldsymbol{r}(u_0, v)$, passing through the point (u_0, v_0), and the corresponding tangent vectors of the two curves are $\partial \boldsymbol{r}/\partial u$ and $\partial \boldsymbol{r}/\partial v$ respectively. So the unit normal vector on the surface patch can be defined as

$$n = \pm\left(\frac{\partial \boldsymbol{r}}{\partial u} \times \frac{\partial \boldsymbol{r}}{\partial v}\right) \Bigg/ \left|\frac{\partial \boldsymbol{r}}{\partial u} \times \frac{\partial \boldsymbol{r}}{\partial v}\right| \tag{28}$$

where $\partial r/\partial u$ and $\partial r/\partial v$ are evaluated at $u = u_0$ and $v = v_0$. We choose the positive sign as our general direction. Fig. 11 shows the normal vector of a sphere and the body surface.

B. Dimension Reduction

There are no appropriate 3-D methods to register the surface voxels of two deformed objects. The 3-D registration of two object surfaces can be treated as a correspondence problem between two sets of surface voxels, which can be simplified as 2-D correspondence problem by using the dimension reduction in both the space domain and the attribute domain.

1) Space Domain Reduction: The 3-D surface generated from contour points on a sequence of slices can be viewed as an elastic web. As mentioned in Section II, the number of selected points on each contour of different PET emission slices is the same. We can cleave the surface at several points and then stretch it into a 2-D rectangle array. Each cell in the rectangular array corresponds to the location of one 3-D surface voxel. The number of cells in each row is equivalent to the number of points on each contour and the number of

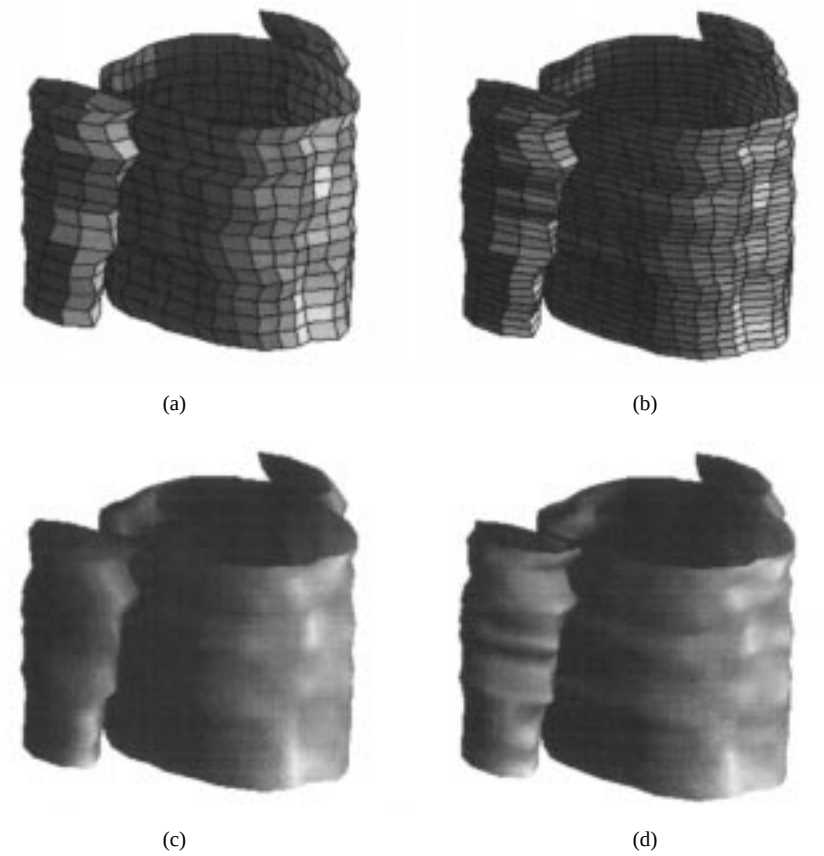

(a) (b)

(c) (d)

Fig. 10. (a) The 3-D surface stacking from the original 15 slices PET imaging contours. (b) The interpolation result which has 30 slices. (c) The original 3-D surface after shading. (d) The interpolation result after shading.

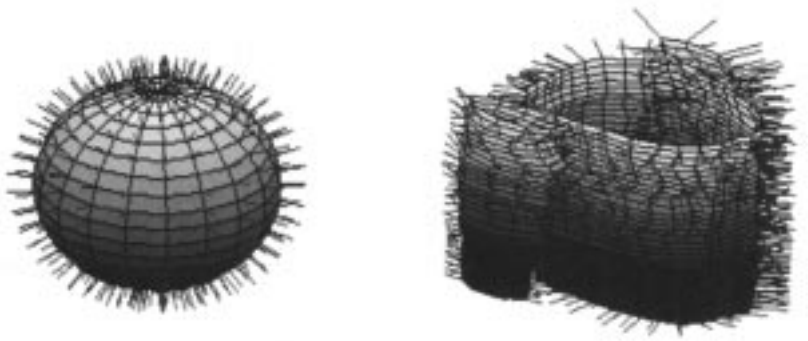

(a) (b)

Fig. 11. (a) Normal vector of a sphere. (b) Normal vector of a body surface.

cells in each column is equivalent to the number of slices. The rectangular array is called the domain frame and is defined as $\Gamma = \{(m,r)(1 \le m \le M, 1 \le r \le R\}$ where M is the number of points on one slice, and there are R slices.

2) Attribute Domain Reduction: Since the normal vector of each surface point is a unit length, there are actually two degrees of freedom in the 3-D normal vector field. Transformation from Cartesian coordinate to Polar coordinate, i.e., $(n_x, n_y, n_z) \rightarrow (\theta, \phi, 1)$, and neglecting the unit length, we can reduce the 3-D coordinate of surface voxels to 2-D coordinate of pixels, i.e., $\{(x,y,z)\} \rightarrow \{(m,r)\}$, and convert the normal direction attribute, i.e., $\{(n_x, n_y, n_z)\} \rightarrow \{(\theta, \phi)\}$. Therefore, at time instance t, the normal vector field can be described as

$$MV(m,r,t) = \{(\theta(m,r,t), \phi(m,r,t)) | (m,r) \in \Gamma, t = n\Delta t\} \quad (29)$$

where Γ is the 2-D domain space and (θ, ϕ) is the attribute space. The 3-D normal direction vector field N can be replaced by the 2-D attribute field MV as

$$N = \{n_x(x,y,z), n_y(x,y,z), n_z(x,y,z))\} \rightarrow MV(m,r,t) = \{(\theta(m,r,t), \phi(m,r,t))\} \quad (30)$$

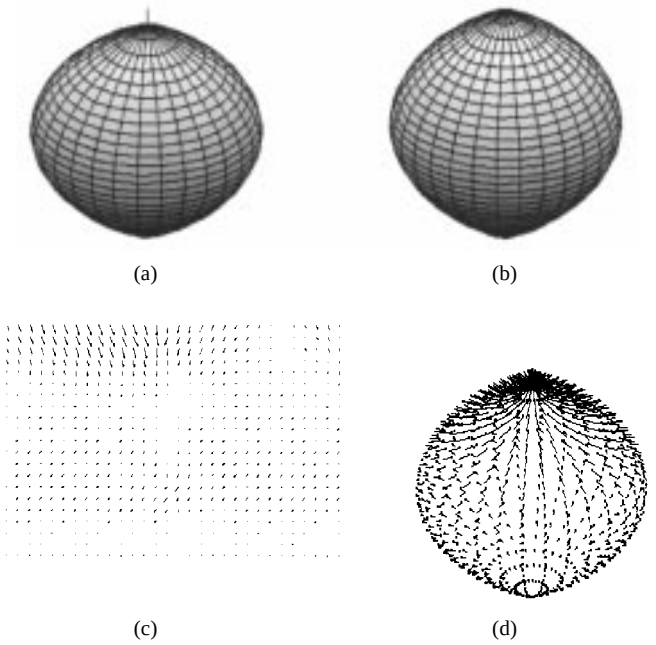

Fig. 12. (a) The original 3-D surface. (b) The reference surface which (a) will deform to. (c) The 2-D displacement vectors of each cell. (d) The deprojected 3-D displacement vector.

where $\{(\theta(m,r,t),\phi(m,r,t))\}$ are the attribute frames of the surface. To register two different object surfaces can be described as a correspondence problem between two attribute frames as $\{(\theta(m,r,t),\phi(m,r,t))\}$ and $\{(\theta(m,r,t+\Delta t),\phi(m,r,t+\Delta t))\}$.

C. Estimate 2-D Correspondence Vector

Since PET images are scanned with all patients in a similar position and the reconstructed surfaces of the 3-D emission scan from different patients resemble each other, we can assume that the normal vector fields of these surfaces change smoothly. Here, we treat the normal vector fields of the reference set and the target set as two sets of two attributes, θ and ϕ, evaluated at t and $t+\Delta t$, respectively. Therefore, the registration problem can be treated as the surface deformation. By using the *normal flow constraint* [17] we can estimate the 2-D correspondence vector field.

There are two constraints in the normal flow method. The first one is *normal flow constraint* which states that the variations of the two attribute frames $\{\theta(m,r,t)\}$ and $\{\phi(m,r,t)\}$ are constant for a small time interval δt which can be described as

$$\theta_m u+\theta_r v+\theta_t=0 \quad \text{and} \quad \phi_m u+\phi_r v+\phi_t=0 \tag{31}$$

where $\theta_m=\partial\theta/\partial m,\theta_r=\partial\theta/\partial r,\theta_t=\partial\theta/\partial t,\phi_m=\partial\phi/\partial m,\phi_r=\partial\phi/\partial r,\phi_t=\partial\phi/\partial t$, and the correspondence vectors are $u=dm/dt$ and $v=dr/dt$. The time derivative is estimated by the variation of the attribute frames of two subjects. Since there are two equations and we can determine the correspondence vectors u and v uniquely from the above equation. However, we have to consider another constraint, the *smoothness constraint*, which dictates that the displacement field changes smoothly in most parts of the frame. Here, we measure the displacement field's departure from smoothness as

$$C_s=\int((y_m^2+u_r^2)+(v_m^2+v_r^2))\,dm\,dr \tag{32}$$

where $u_m=\partial u/\partial m,u_r=\partial u/\partial r,v_m=\partial v/\partial m$, and $v_r=\partial v/\partial r$ are the partial gradients of the two components of the displacement velocity. The error of the *normal flow constraint* can be described as

$$C_{c\theta}=\int(\theta_m u+\theta_r v+\theta_t)^2\,dm\,dr. \tag{33}$$

These two constraints are described by two measurements which are combined as the energy function $W_\theta=C_s+\lambda_\theta C_{c\theta}$, where λ_θ is a weighting factor for the attribute frame $\{\theta(m,r,t)\}$. The energy function is to be minimized to obtain the correspondence vector field between two attribute frames at two time instance. However, there is another attribute frame $\{\phi(m,r,t)\}$. Similarly, we need to consider the second energy term $W_\phi=C_s+\lambda_\phi C_{c\phi}$ where $C_{c\phi}=\int\int(\phi_m u+\phi_r v+\phi_t)^2\,dm\,dr$. The total energy function needs to be minimized in the linear combination of W_θ and W_ϕ. Minimizing an integral of the form $\int F(u,v,u_m,u_r,v_m,v_r)\,dm\,dr$ is a problem of the calculus of variation. We can approximate the minimization problem with a finite difference scheme to obtain the solution [21].

D. 3-D Correspondence Vector Deprojection

The generated 2-D correspondence vector field (i.e., $\{MV'\}$) cannot be applied to find the correspondence between two sets of 3-D surface voxels. Here, we need to deproject the 2-D correspondence vector field to the 3-D vector field (i.e., $\{MV\}$) which indicates the surface deformation between two sets of PET emission scan data. Given a 2-D correspondence vector, $MV'(=(u,v))$ (located on a small grid), we need to find the 3-D correspondence vector $MV(=(x,y,z))$ on the 3-D surface. $P1',P2',P3'$, and $P4'$ are the corner points of the 2-D grid (i.e., located at $(u_1,v_1),(u_2,v_2),(u_3,v_3),(u_4,v_4)$), and the corresponding points of these corner points on the 3-D surface patches are $P1,P2,P3$, and $P4$ (i.e., located at $(x_1,y_1,z_1),(x_2,y_2,z_2),(x_3,y_3,z_3),(x_4,y_4,z_4)$) which are not on the same plane. Assume that these corner points are close enough, so we can develop a method to find the 3-D correspondence vector.

For each MV' (pointing to (u,v) on the 2-D plane, there is a corresponding MV pointing to (x,y,z) on the 3-D surface which can be derived as,

$$Rv=v-v_1 \quad \text{and} \quad Ru=u-u_1. \tag{34}$$

Then, using Rv, the coordinates of point A and B can be determined as

$$(x_A,y_A,z_A)=(x_1,y_1,z_1)+Rv\cdot((x_4,y_4,z_4)-(x_1,y_1,z_1)) \tag{35}$$

$$(x_B,y_B,z_B)=(x_2,y_2,z_2)+Rv\cdot((x_3,y_3,z_3)-(x_2,y_2,z_2)). \tag{36}$$

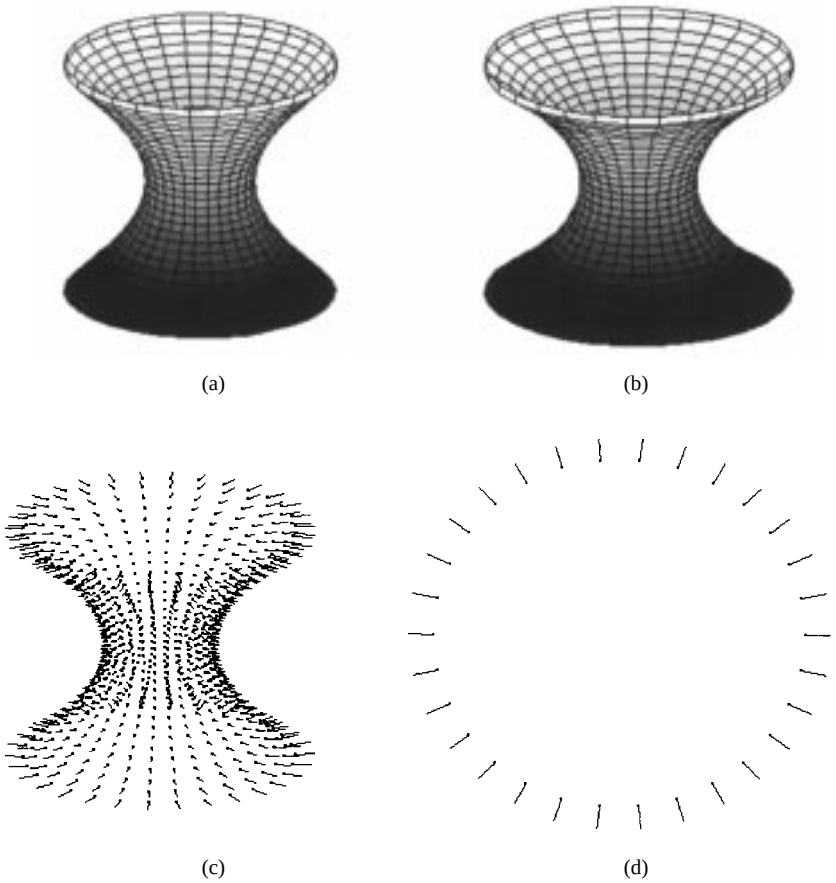

Fig. 13. (a) The original cylinder. (b) The reference cylinder whose cross-section area is larger than (a). (c) The 3-D displacement vectors of each surface point. (d) The top-view of the 3-D displacement vectors.

Finally, the 3-D correspondence vector is approximated by

$$(x, y, z) = (x_A, y_A, z_A) + Ru \cdot ((x_B, y_B, z_B) - (x_A, y_A, z_A)). \quad (37)$$

E. The Registration Results

In the first test, we used two synthesis spheres. The two spheres with their center located at the origin and treated as one sphere deformed at two time instances. Fig. 12(a) shows the first sphere which has 28 circular slices and then it is deformed as the second sphere which has 30 circular slices as shown in Fig. 12(b). Fig. 12(c) shows the 2-D correspondence vectors of each cell. From these figures, we find that most correspondence vectors are upward especially on the upper columns. This is correct as we compare the original two surfaces. Fig. 12(d) shows the deprojected 3-D correspondence vector of each surface point. These correspondence vectors are moving upward and outward at the upper surface points.

In the second test, we use two synthesized solids-of-revolution with different cross section as the deformed object at two time instance. The smaller one is shown in Fig. 13(a), and the larger one is demonstrated in Fig. 13(b). The smaller one is deformed and becomes the larger one. From the estimated 3-D correspondence vectors [shown in Fig. 13(c)], we find that the correspondence vectors are moving outward. The top-view of the correspondence field of one slice is shown in Fig. 13(d).

Finally, we use the real 3-D surfaces extracted from the PET emission scan imaging to test the correspondence vector estimation method. Fig. 14(a) shows the 3-D surfaces generated from the target set and Fig. 14(b) shows those generated from the reference set. The 3-D residual displacement vectors of each surface point are shown in Fig. 14(c). The global translation vectors of each surface are eliminated from the estimated 3-D correspondence vectors. Fig. 14(d) shows the 3-D surfaces reconstructed by using the 3-D correspondence vectors. Comparing Fig. 14(b) and (d), we find that they closely resemble each other.

V. Transmission Scan Synthesis

Using the correspondence vectors at each surface point, we may synthesize the PET transmission scan of the reference set. Here, we modify the 2-D interpolation method [22] for our 3-D application. There are two procedures: 1) The *correspondence vector interpolation* uses the correspondence vectors on boundary contours of two slices to generate the correspondence vector field for the interior part of the cross-section area in each slice. 2) The *graylevel interpolation* applies the correspondence relation between two emission scans and uses the transmission scan of the reference set to synthesize the transmission scan of the target set.

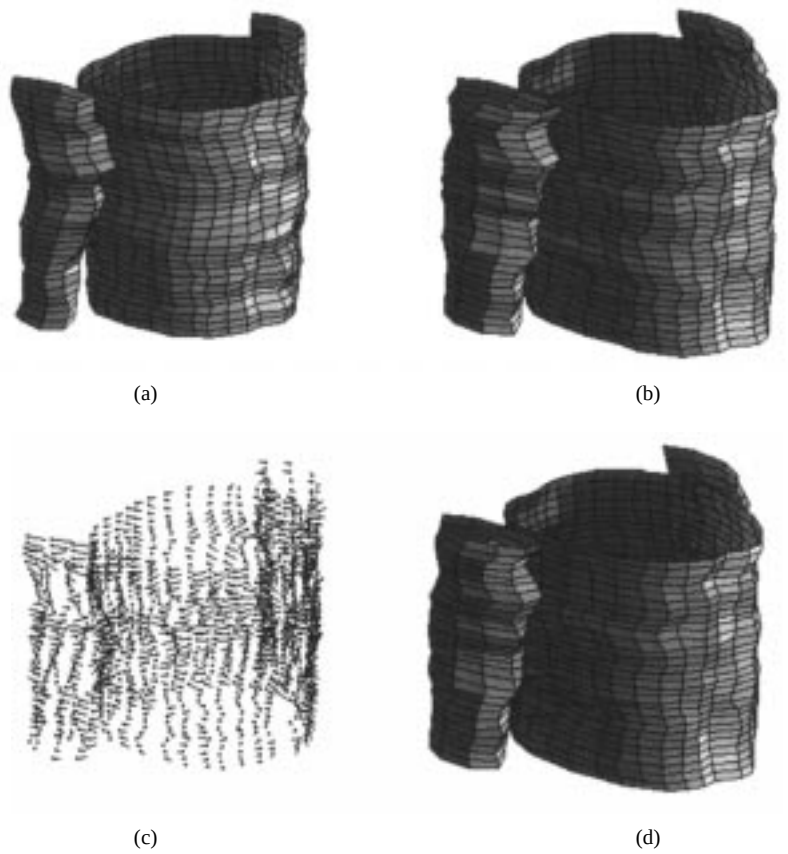

(a) (b) (c) (d)

Fig. 14. (a) The 3-D surface of body shape generated from the target set. (b) The 3-D surface of the reference set. (c) The estimated 3-D displacement vectors of each surface point. (d) The deformed 3-D surface which is similar to the reference one.

A. 3-D Correspondence Vector Interpolation

Each grid point on the boundary of the target set has a 3-D correspondence vector which can be viewed as a mapping between the point in the emission scan of the reference set and the corresponding point in the emission scan of the target set. The correspondence vector field is represented as a global correspondence vector and a local residual vector field.

The residual 3-D correspondence vector at the surface point is described as

$$\boldsymbol{MV}_i = (x_i - x_{\text{mean}}, y_i - y_{\text{mean}}, z_i - z_{\text{mean}}). \tag{38}$$

where $(x_{\text{mean}}, y_{\text{mean}}, z_{\text{mean}})$ is the correspondence vector of the center of the contour. Then the correspondence vector at each grid point inside the interior part of the cross-section region of each slice (i.e., z component is a constant) can be interpolated as

$$GV(x,y,z) = \sum_{i=1}^{N} W_i MV_i \Big/ \sum_{i=1}^{N} W_i \tag{39}$$

where

$$W_i(x,y) = \exp \frac{-[(x-x_i)^2 + (y-y_i)^2]^{1/2}}{\beta}$$

is a weighting factor similar to the Gaussian function based on the distance between the grid point and the surface point on the same slice. The value of β is chosen manually and it depends on the amount of deformation between the two image pairs. If one contour is very distorted compared to the other, we will use a larger value of β to interpolate the correspondence vector field. The interpolated correspondence vector field will be closer to the global correspondence vector. But if the contour is close to the real boundary of the body, we will use a smaller value of β to generate the correspondence vector concerning a local area.

In Fig. 15, each slice is separated into four sections: three contour sections and one background section. The correspondence vectors of the points inside each contour section are interpolated from the correspondence vectors on the boundary contour of the same contour section, but the correspondence vectors of the points in the background section are extrapolated from the correspondence vectors on the boundary contours of all three sections. Fig. 15(a) illustrates the x and y components of the 3-D correspondence vectors of the boundary points on one slice and Fig. 15(b) shows the interpolated correspondence vectors inside the interior part of the three contour sections.

B. Graylevel Interpolation

The 3-D correspondence vectors indicate the mappings from one emission scan to another emission scan. However, these mappings do not map integer points to integer points. We can not use these mappings to synthesize the target transmission scan from the reference transmission scan. The intensity value of each point on the target transmission scan is mapped to a noninteger point on the reference transmission scan which

(a) (b)

Fig. 15. (a) The displacement vectors on the three contours. (b) The interpolated displacement vectors inside the contours.

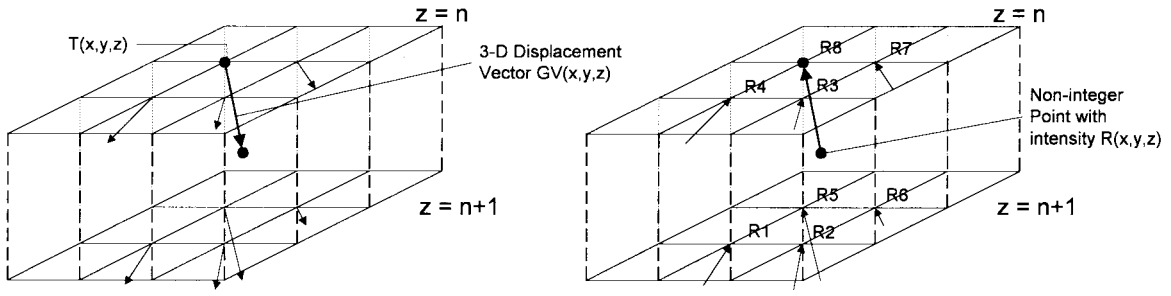

(a) (b)

Fig. 16. (a) The synthesized transmission scan of the target set. (b) The original transmission scan of the reference set. The intensity of the noninteger point $R(x, y, z)$ is interpolated by the neighboring integer points R1–R8.

must be interpolated by the neighboring integer points. The graylevel of this noninteger point can be determined by its eight neighboring points. Here, we use a 3-D Gaussian weighting function to interpolate the graylevel as

$$T(x,y,z) = \sum_{i=1}^{8} W_i R_i \Big/ \sum_{i=1}^{8} W_i \tag{40}$$

where

$$W_i = \exp \frac{-[(x-x_i)^2 + (y-y_i)^2 + (z-z_i)^2]^{1/2}}{\sigma}$$

and $\{R_i | i = 1, \cdots, 8\}$ are the intensities of the eight neighboring integer points of the noninteger point located at (x, y, z) with intensity $R(x, y, z)$. $T(x, y, z)$ is the intensity of the integer point on the slice n of the synthesized transmission scan, where $T(x, y, z) = R(x, y, z)$. The shorter distance to its neighbors is found, the larger weighting W_i will be generated, it indicates a greater influence of its neighbor on the interpolation. Fig. 16 illustrates that the noninteger point $R(x, y, z)$ is interpolated by the neighboring eight integer points.

VI. Experiment Results and Discussion

We have successfully developed a registration method to register two different PET emission scan images (see Figs. 17 and 18). The results of this intersubject registration are applied on the transmission scan synthesis. By using the 3-D correspondence vector and graylevel interpolation on the transmission scan scans of the reference set, we can synthesize the transmission scans of the target set. Figs. 19 and 21 show the original transmission scan and the synthesized one. If we apply the conventional correlation-based method to register the centroid [5] for each slice of the emission scan of the reference set (Fig. 17) and the emission scan of the target set (Fig. 18). These registration parameters are then applied to adjust the transmission scan for intersubject transmission scan substitution. However, by comparing the adjusted transmission scan and the original genuine transmission scan, we find that their difference (Fig. 22) is much worse than the difference between the synthesized transmission scan and the original transmission scan (Fig. 23).

From Figs. 22 and 23, we find that the difference on the neighborhood of the boundary of body is trivial by using our method. However, the difference inside the body is obvious. This is because the tissue inside the body of one subject is different from the other's. Here, we only use boundary information to synthesize the transmission scan, so that the graylevel inside the body cannot be determined efficiently by this method. If we can get the information inside the body, this problem will be improved and the difference inside the body will be reduced. To verify our results, we use the same method to register two original transmission scan images (Figs. 19 and 20) instead of two emission scan images. The estimated 3-D correspondence vectors and the interpolation results should have been more accurate. However, we find that the improvement is limited since the difference inside the body can not be reduced effectively. The difference images are illustrated in Fig. 24.

Table I shows the signal-to-noise ratio (SNR) and mean-square error (MSE) of the experimental results. In the body scan images, the first experiment illustrates the difference by using the correlation-based centroid registration on the two emission scans of the reference set and the target set. The average SNR of this case is about 11.3 dB. The next experiment shows the difference by utilizing the emission scans registration, and the average SNR of the difference

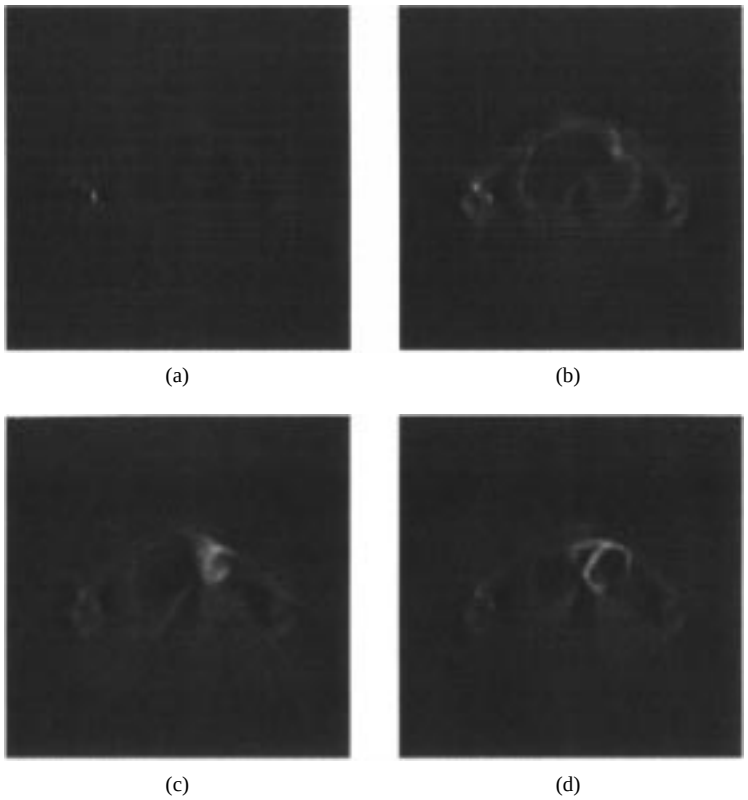

(a) (b) (c) (d)

Fig. 17. The (a) first, (b) fourth, (c) seventh, and (d) tenth slices of the PET emission scan of the target set.

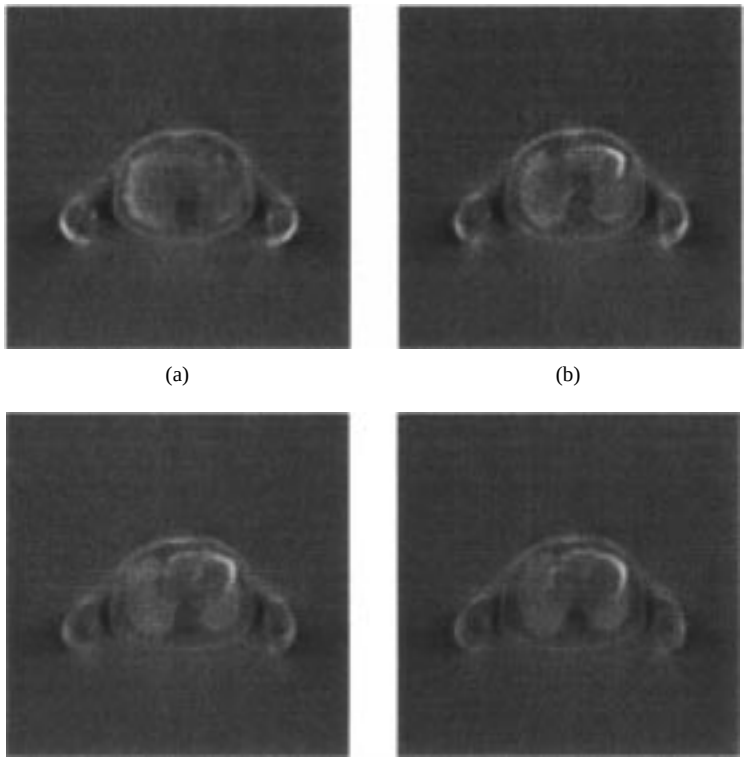

(a) (b) (c) (d)

Fig. 18. The (a) first, (b) fourth, (c) seventh, and (d) tenth slices of the PET emission scan of the reference set.

between the synthesized transmission scan and the real one is about 14.8 dB. The third experiment indicates the difference by applying the registration algorithm to two transmission scans, and the average SNR is about 15.9 dB. So, the emission scans registration and the transmission synthesis that we have proposed do decrease the difference between the real transmission scan and the corresponding synthesis one. Comparing the first and second experiments, we find that our algorithm

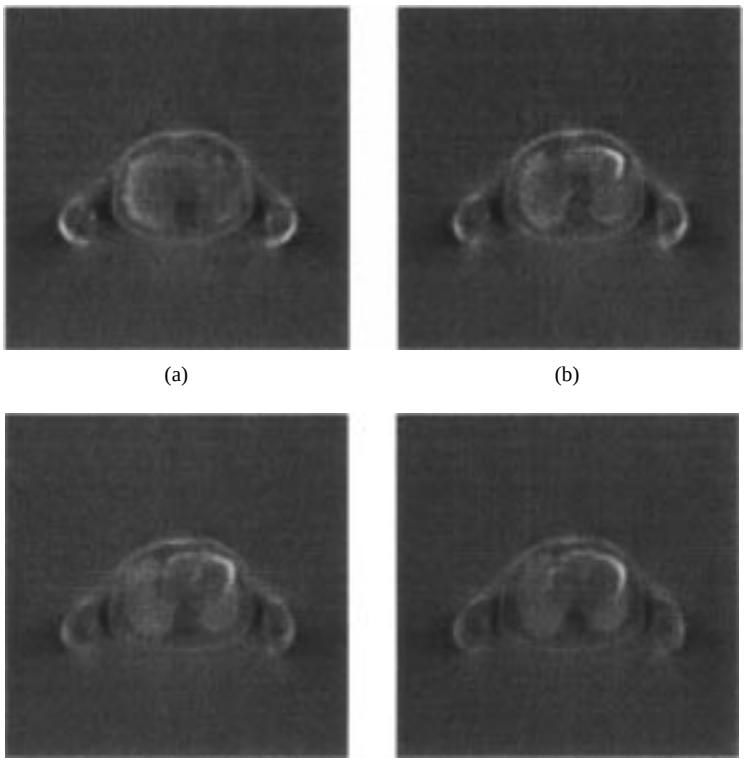

(a) (b) (c) (d)

Fig. 19. The (a) first, (b) fourth, (c) seventh, and (d) tenth slices of the original transmission scan of the target set.

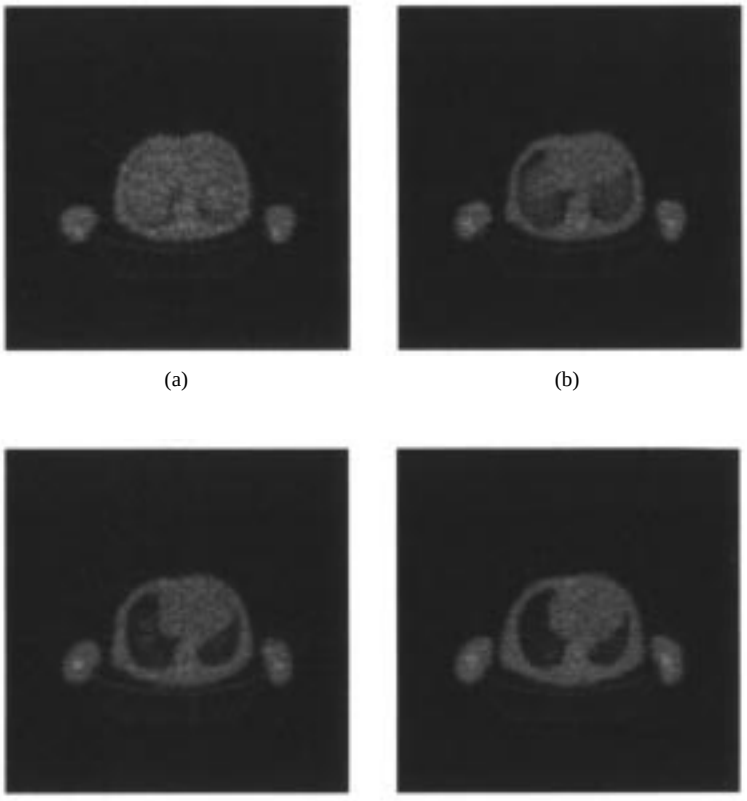

(a) (b) (c) (d)

Fig. 20. The (a) first, (b) fourth, (c) seventh, and (d) tenth slices of the transmission scan of the reference set.

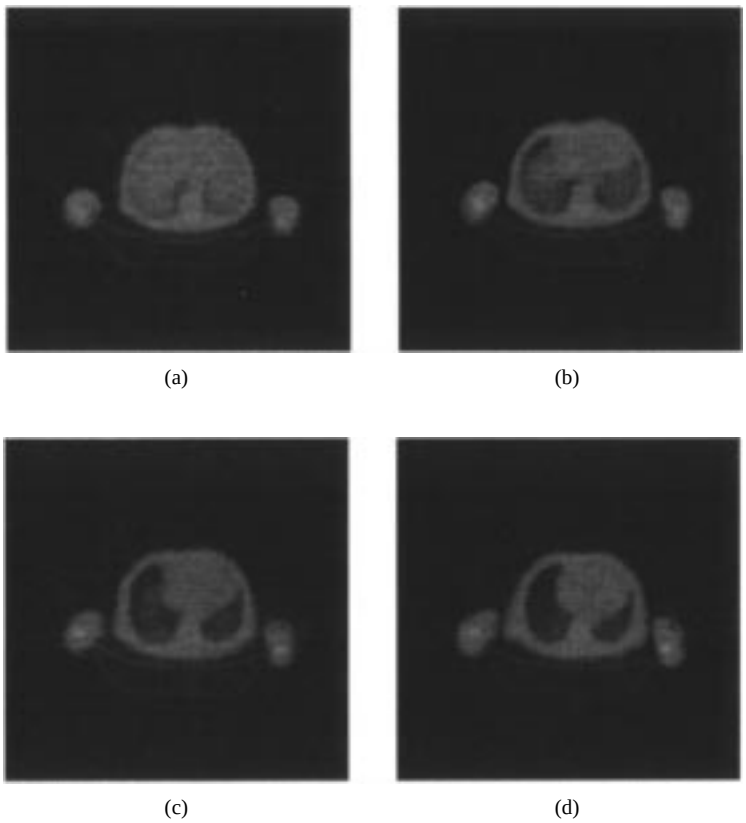

(a) (b)

(c) (d)

Fig. 21. The (a) first, (b) fourth, (c) seventh, and (d) tenth slices of the synthesized transmission scan of the target set.

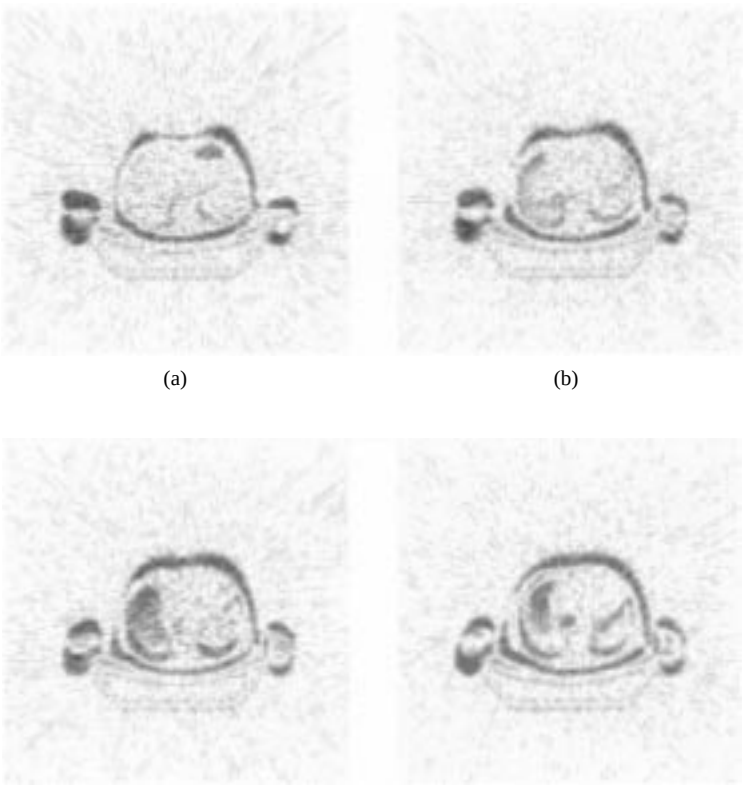

(a) (b)

(c) (d)

Fig. 22. The (a) first, (b) fourth, (c) seventh, and (d) tenth slices of the original transmission scans of the target set and the reference set (i.e., with centroid registration).

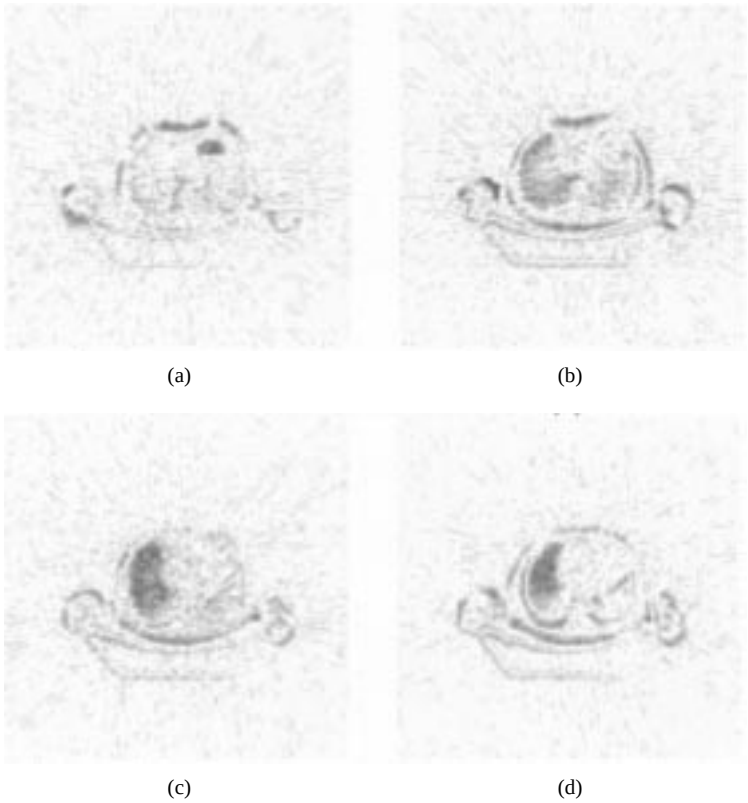

(a) (b)

(c) (d)

Fig. 23. The (a) first, (b) fourth, (c) seventh, and (d) tenth difference slices of the synthesized transmission scan and the original transmission scan of the target set. The registration is applied on the two corresponding precorrected PET emission scan image.

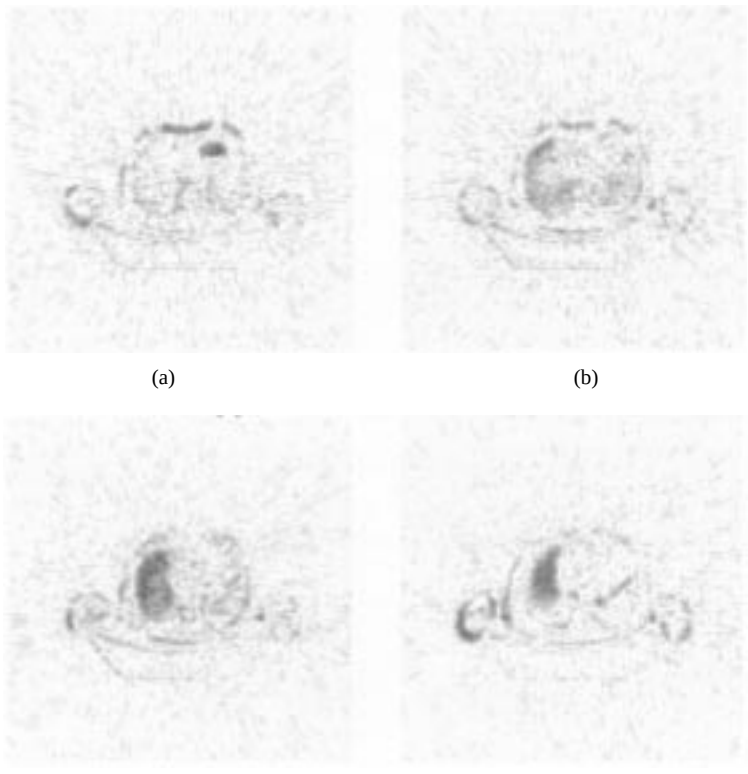

(a) (b)

(c) (d)

Fig. 24. The (a) first, (b) fourth, (c) seventh, and (d) tenth difference slices of the synthesized result and the original transmission scan. The registration is applied on the two original transmission scan images.

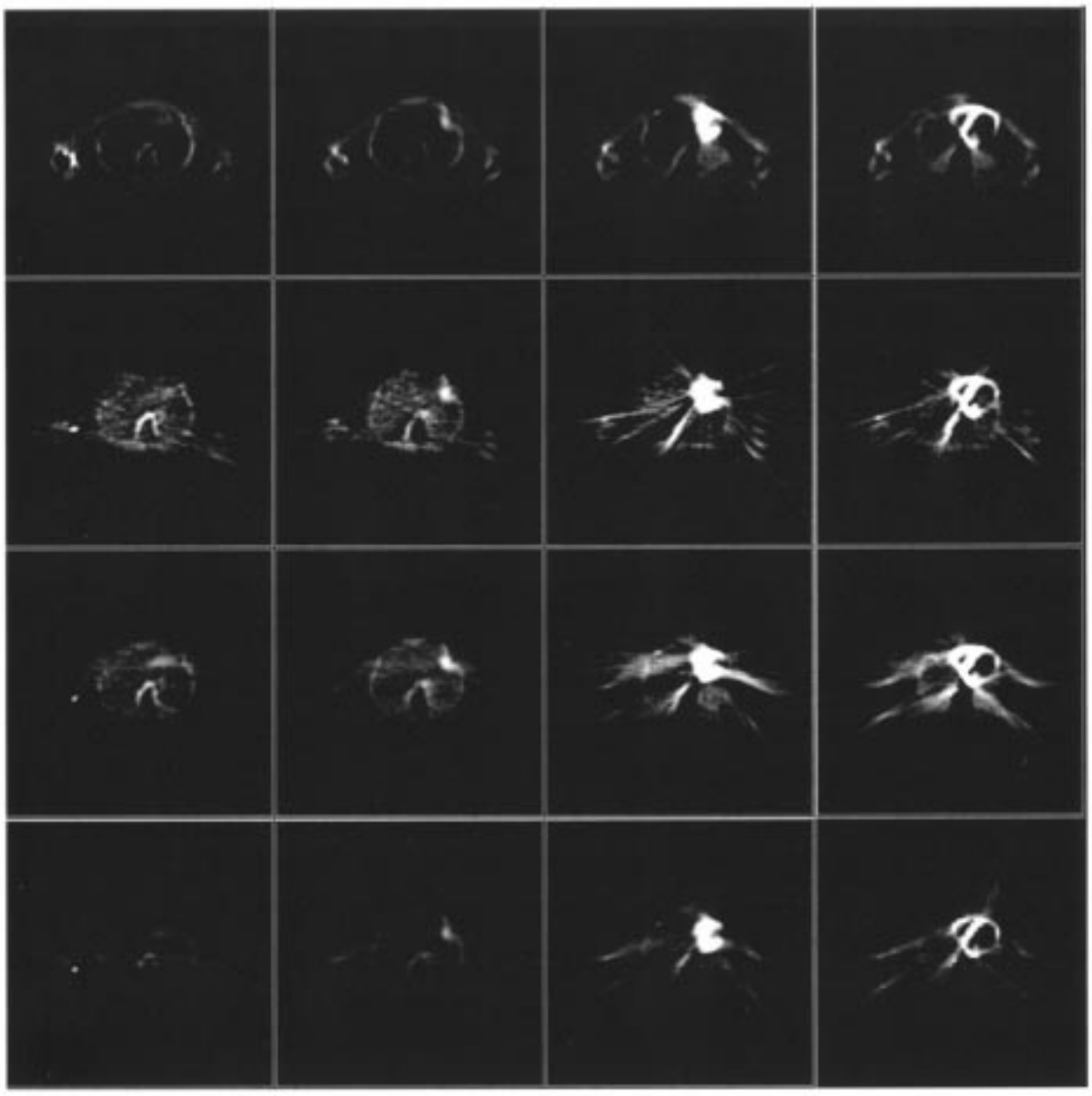

Fig. 25. The first, fourth, seventh, and tenth slices of the emission scan data: a) the first row is the emission scan images without attenuation correction (AC), b) the second row is the emission scan images with AC using the original transmission data, c) the third row is the emission scan images with AC using the synthesized transmission data, d) the fourth row is the emission scan images with AC using the contour information only.

TABLE I
THE EXPERIMENT RESULTS OF THE DIFFERENCE BETWEEN TWO SETS OF THE TRANSMISSION SCAN IMAGES

Methods	Controid Registration (Fig. 22)		Registration using Emission Scans (Fig. 23)		Registration using Transmission Scans (Fig. 24)	
Average Difference	SNR(dB)	MSE	SNR(dB)	MSE	SNR(dB)	MSE
	11.27	307.20	14.76	137.58	15.86	106.71

does improve the SNR by 3.5 dB. The results of the second experiment are very close to the third experiment with only 1.1 dB less.

To illustrate that our synthesized transmission data provides an acceptable attenuation correction information for the target emission scan, we do the following operations: 1) project the synthesized transmission image to generate the attenuation correction projections, 2) measure the emission projection using PET scanner, 3) do the emission attenuation correction of the emission scan projection using these attenuation correction projections, and 4) reconstruct the 2-D emission scan images. Then, to justify our new approach by comparing the different attenuation data for attenuation correction of the same emission scan, we propose the following three methods: a) using the

original transmission scan for attenuation correction, b) using the synthesized transmission scan for attenuation correction, and c) using the outer contour only for attenuation correction (provided by the Scandritronix). The contour method provided by Scanditronix assumes uniform attenuation inside the contours. In this experiments, the attenuation coefficient is assigned as 0.096 1/cm for the reconstruction software. The results of the attenuation corrected emission scan data are illustrated in Fig. 25 from which we can find that using our method [i.e., method b)] to do the attenuation correction may have image quality of the corrected emission scan very close to the results of method a) and better than the results of method c). Especially in the lower slices (from first to fourth slices), we find very little distortion generated because there are less nonhomogeneous internal organs (i.e., no heart and no lungs are seen in these slices).

From the experimental results, we may find that our method can provide an effective synthesized attenuation correction data for the PET emission scans attenuation correction. The quality of the attenuation corrected PET emission images is subjectively acceptable. However, it is only suitable for some PET image scans such as midriff or brain in which there are no significant internal organs. Our method only uses the intersubject body boundary information which can be applied to register the intersubject contours and then synthesize the attenuation correction data accurately. The information inside the body can also be synthesized correctly if the interior organs of the body can extracted and then registered accurately. However, in the real case, how to extract the interior organs' contour of the precorrected PET emission scan is a nontrivial problem because of the poor image quality of the emission scan imaging.

VII. Conclusions

Due to the poor image quality of the PET precorrected emission scan, we have developed a system using PDM to extract the boundary of human body scan images. Then we utilize the boundary information to register the emission scans, and synthesize a new transmission scan of the target set from the registered correspondence vectors. In the near future, we are studying how to extract the internal organs inside the emission scan accurately. The nontrivial problem still remain to be solved, which requires the help from a more advanced PET emission imaging technique for making clearer emission scan images.

References

[1] M. Herbin, A. Venot, J. Devaux, E. Walter, J. Lebruchec, L. Dubertret, and J. Roucayrol, "Automated registration of dissimilar images: Application to medical imagery," *Comput. Vision, Graphics, Image Processing.*, vol. 47, pp. 77–88, 1989.

[2] D. C. Barber, "Registration of low resolution medical images," *Phys. Med, Biol.*, vol. 37, no. 7, pp. 1485–1498, 1992.

[3] R. P. Woods, S. R. Cherry, and J. C. Mazziotta, "Rapid automatic algorithm for aligning and reslicing PET images," *J. Comput. Assist. Tomogr.*, vol. 14, no. 4, pp. 620–633, 1992.

[4] S. L. Bacharach, M. A. Douglas, R. E. Carson, P. F. Kalkowski, N. Freedman, P. Perrone-Filardi, and R. O. Bonow, "Three-dimensional registration of cardiac PET attenuation scans," *J. Nucl. Med.*, vol. 34, no. 2, pp. 311–321, Feb. 1993.

[5] P. Thevenaz, U. E. Ruttimann, and M. Unser, "Iterative multi-scale registration without landmarks," *IEEE Workshop Biomed. Image Anal.*, 1995, pp. 228–231.

[6] C. A. Pelizzari, G. T. Y. Chen, D. R. Spelbring, R. R. Weichselbaum, and C. T. Chen, "Accurate three-dimension registration of CT, PET, and/or MR images of the brain," *J. Comput. Assist. Tomogr.*, vol. 13, no. 1, pp. 20–26, 1989.

[7] M. E. McCord, S. L. Bacharach, R. O. Bonow, V. Dilsizian, A. Cuocolo, and N. Freedman, "Misalignment between PET transmission and emission scans: Its effect on myocardinal imaging," *J. Nucl. Med.*, vol. 33, pp. 1209–1214, 1992.

[8] A. C. Evans, S. Marrett, L. Collins, and T. M. Peters, "Automatical functional correlative analysis of the human brain using three dimensional imaging systems," in *Proc. SPIE Conf. Medical Imaging III: Image Processing*, 1989, vol. 1092, pp. 264–274.

[9] N. M. Alpert, J. F.Bradshaw, D. Kennedy, and J. A. Correia, "The principal axes transformation—A method for image registration," *J. Nucl. Med.*, vol. 31, no. 10, pp. 1717–1722, Oct. 1990.

[10] P. A. Van den Elsen, J. B. A. Maintz, E.-J. D. Pol, and M. A. Viergever, "Automatic registration of CT and MR brain images using correlation of geometrical features," *IEEE Trans. Med. Imag.*, vol. 14, no. 2, pp. 384–396, June 1995.

[11] L. Thurfjell, C. Bohm, T. Greitz, and L. Eriksson, "Transformations and algorithm in a computerized brain atlas," *IEEE Trans. Nucl. Sci.*, vol. 40, no. 4, pp. 1187–1191, Aug. 1993.

[12] K. P. Lin, "Methods for automated registration of intra- and inter-subject tomographic images," Ph.D. dissertation, Univ. California, Los Angeles (UCLA), 1994.

[13] C. Davatzikos and J. L. Prince, "Brain image registration base on curve mapping," *IEEE Workshop Biomed. Image Analysis*, 1994, pp. 245–261.

[14] S. Eberl, I. Kanno, R. R. Fulton, A. Ryan, B. F. Hutton, and M. J. Fulham, "Automatic inter-study image registration technique for SPECT and PET," *J. Nucl. Med.*, vol. 37, no. 1, pp. 137–145, Jan. 1996.

[15] T. F. Cootes, A. Hill, C. J. Taylor, and J. Haslam, "Use of active shape models for locating structures in medical images," *Image, Vision Computing*, vol. 12, no. 6, pp. 355–365, 1994.

[16] T. F. Cootes, C. J. Taylor, D. H. Cooper, and J. Graham, "Active shape models-their training and application," *Comput. Vision, Image Understanding*, vol. 61, no. 1, pp. 38–59, Jan. 1995.

[17] I. C. Chang, C. L. Huang, C. C. Lien, L.C. Wu, and S. H. Yeh, "Left ventricular motion analysis of 4-D SPECT imaging using normal direction constraint," *IEICE Trans. Inform. Syst.*, vol. E77-D, no. 11, 1994.

[18] D. J. Burr, "Elastic matching of line drawing," *IEEE Trans. Pattern Anal. Machine Intell.*, vol. PAMI-3, no. 6, pp. 708–713, 1981.

[19] R. C. Gonzalez and R. E. Woods, *Digital Image Processing*, Reading, MA: Addison-Wesley, 1992.

[20] J. C. Gower, "Generalized Procrustes analysis," *Psychometrika*, vol. 40, pp. 33–51, 1975.

[21] B. K. P. Horn, *Robot Vision*. Cambridge, MA: The MIT Press, 1986.

[22] M. Moshfeghi, "Elastic matching of multi-modality medical images," *Comput. Vision Graphics, Image Processing*, vol. 53, no. 3, pp. 271–282, May 1991.

[23] A. Deruyver and Y, Hode, "Automatic multi-thresholdable image segmentation by using separation bipoints," in *Proc. 13th Int. Conf. Pattern Recogn.*, Vienna, Austria, 1996, vol. II, pp. 457–461.

[24] M. J. D. Powell, "An efficient method for finding the minimum of a function of several variables without calculating derivatices," *Comput. J.*, vol. 7, pp. 155–163, 1964.